# **Geophysical Journal International**

Royal Astronomical Society

Geophys. J. Int. (2025) 243, 1–26 Advance Access publication 2025 September 8 Research Paper https://doi.org/10.1093/gji/ggaf351

# First-order control factors for ocean-bottom ambient seismology interferometric observations

Adesh Pandey<sup>®</sup>, Jeffrey Shragge<sup>®</sup> and Aaron J. Girard<sup>®</sup>

Center for Wave Phenomena, Department of Geophysics, Colorado School of Mines, Golden, CO 80401, USA. E-mail: adesh0805@gmail.com

Accepted 2025 August 30. Received 2025 August 25; in original form 2025 March 25

### SUMMARY

Expanding the lower-frequency band of seismic energy sources, particularly below 2.0 Hz, is crucial for improving the stability and effectiveness of full waveform inversion (FWI). Conventional active sources including airguns are ineffective at generating low-frequency wavefields, while ambient seismic wavefields, driven by natural energy sources such as ocean waves, offer a promising alternative. Effectively using ambient wavefield energy for seismic imaging or inversion analyses, though, requires understanding key physical control factors contributing to observations—including ambient source mechanisms and distribution, oceanbottom bathymetry and Earth model heterogeneity—which influence wave-mode excitation and partitioning, particularly in the context of ocean-bottom ambient seismic interferometry. This study presents a modelling framework for simulating cross-correlation wavefields generated by ambient seismic sources for dense ocean-bottom sensor arrays within a coupled acoustic-elastic system, without relying on Green's function retrieval assumptions. We model velocity and pressure cross-correlation wavefields to explore the effects of ocean-bottom velocity structure, ambient source distributions and bathymetric variations on seismic wave excitation and propagation in the low- (0.01-2.00 Hz) frequency band. Our results show that the distribution of ambient energy source locations, whether at the seabed or sea surface, significantly affects excited wave-mode characteristics. Love waves are particularly evident in the presence of substantial lateral and vertical bathymetric variations and heterogeneous Earth structure. The distribution of azimuthal ambient energy sources also influences Love-wave excitation, with the most prominent waves observed in the direction of the highest source concentration. Additionally, different particle velocity component and pressure virtual shot gathers exhibit varying sensitivity to surface waves. This work improves the understanding of low-frequency ambient seismic wavefields in ocean environments, with potential applications in long-wavelength structural imaging and elastic velocity model estimation for FWI analysis.

**Key words:** Seismic interferometry; Seismic noise; Guided waves; Surface waves and free oscillations; Wave propagation.

#### 1 INTRODUCTION

Recent advancements in multicomponent ocean-bottom sensor array deployments—including ocean-bottom seismometers (OBSs), cables (OBCs) and nodes (OBNs)—offer a unique opportunity for investigating marine ambient wavefield phenomena. When deployed in sparse (4–16 stations per km²), large-scale (>100 km²) arrays on the seafloor, these instruments enable the extraction and analysis of low-frequency (sub-2.0 Hz) wavefield information. Although primarily designed for active-source seismic exploration, continuous ocean-bottom recordings spanning one to three months often capture extensive data below the typical 2.0 Hz low-frequency cut-off of marine airgun sources, effectively extending into the

range beneath the noise floor of the receivers themselves. Traditionally considered 'noise', these seismic data—primarily originating from ambient seismic sources such as ocean swell noise (Longuet-Higgins 1950)—increasingly are being recognized for their potential to provide valuable surface-wave information through ambient seismic interferometry analyses.

As illustrative examples, vertical-vertical and radial-radial components ambient virtual shot gathers (VSGs) derived from OBN recordings in the Astero field in the Norwegian North Sea revealed fundamental and first-order Scholte waves, while the transverse-transverse component indicated the presence of Love waves (Bussat & Kugler 2011). Surface wave tomography of these data yielded Scholte-wave group velocity images at frequencies between 0.18

Stewart (2006)

Ning et al. (2024)

0.15 - 2.0

0.45 - 2.0

Study Area Components Wave types Frequency investigated reported (Hz) Bussat & Kugler (2011) VV, RR, TT 0.18 - 0.40Astero field, Scholte and Love Norwegian North Sea de Ridder & Dellinger (2011). Valhall field. VV. RR. TT. Scholte and Love 0.35 - 1.75de Ridder & Biondi (2013a, b) TR, VR, VT Norwegian North Sea Mordret et al. (2013) Valhall field, VV, TT Scholte and Love 0.4 - 2.0Norwegian North Sea de Ridder & Biondi (2015) Ekofisk field, PP Scholte 0.35 - 1.35Norwegian North Sea Girard et al. (2023) Gulf of Mexico VV. RR. TT. PP Scholte and guided P 0.2 - 1.6Girard et al. (2024) VV, PP Scholte and guided P 0.08 - 1.50Amendment field,

VV, RR, TT, PP

PP

**Table 1.** Summary of VSG observations from notable ocean-bottom deployments, V = Vertical, R = Radial, T = Transverse and P = Pressure.

Gulf of Mexico

Gulf of Mexico

Gulf of Mexico

and 0.40 Hz, correlating well with known subsurface structures. Similarly, permanently deployed OBC arrays at the Valhall field in the Norwegian North Sea revealed fundamental and first-order Scholte wave modes on vertical-vertical VSGs, Love waves on the transverse-transverse VSGs, and facilitated near-surface imaging through Scholte-wave group and phase velocities in the 0.35-1.75 Hz frequency range using straight-ray tomography (de Ridder & Dellinger 2011; Mordret et al. 2013; de Ridder & Biondi 2013a, b). In the Gulf of Mexico, vertical-vertical, radial-radial and pressure-pressure components VSGs from continuous OBN array recordings revealed dispersive Scholte- and guided P-wave modes within the sub-1.2 Hz frequency band (Girard et al. 2023, 2024). Stewart (2006) also demonstrated the presence of Scholte waves on vertical-vertical and transverse-transverse VSGs in the sub-2.0 Hz frequency band and noted that vertical-vertical particlemotion VSGs exhibited the strongest events. Ning et al. (2024) used dispersion estimates derived from pressure-pressure VSGs from a sparse Gulf of Mexico OBN array and observed the fundamental Scholte wave mode in the sub-1.2 Hz frequency band. 1-D Scholte-wave inversion of this data set resulted in shear-wave velocity  $(v_s)$  estimates to 3.0 km depth, that exhibited structural similarity to the compressional-wave velocity  $(v_p)$  model obtained from full waveform inversion (FWI) analysis of active-source seismic OBN data. Table 1 presents a comprehensive summary of these studies. Collectively, they demonstrate the potential of using the low-frequency information recorded in ocean-bottom sensor data for subsurface investigation, complementing conventional seismic exploration analysis.

In FWI analyses, low-frequency seismic data play a crucial role in effectively reducing cycle skipping, leading to faster convergence and stability in FWI analyses (Virieux & Operto 2009). However, obtaining reliable low-frequency information with a high signal-tonoise ratio from sub-2.0 Hz field data remains a significant challenge. As a result, these low frequencies generally are extrapolated from high-frequency active-source seismic data (Li & Demanet 2016). In contrast, ambient oceanic seismic energy is inherently rich in low frequencies (0.05-2.00 Hz) (Longuet-Higgins 1950; Webb 1998; Bromirski et al. 2005), which are difficult to generate with active seismic sources. These low-frequency components potentially can complement active-source seismic data in FWI analyses within the corresponding frequency range for ocean-bottom acquisitions. However, fully exploiting ocean-bottom ambient data for low-frequency elastic model building through FWI requires a comprehensive understanding of the physical factors that influence cross-correlated wavefield observations. This necessitates interpreting ambient wavefield data within a marine environment context characterized by acoustic and elastic media coupled at the seabed and accurately modelling these wavefields within a suitable seismic interferometry framework that accounts for various physical control factors associated with the physical system. Conventional assumptions, such as an isotropic distribution of ambient sourcescommonly used to simplify cross-correlations as approximations of Green's functions—are rarely valid in marine environments. Pandey et al. (2025) shows that a low-frequency, homogeneous source distribution confined to the ocean surface in a coupled acoustic-elastic system—characteristic of a marine environment—fails to recover the correct phases of surface-wave modes recorded on OBNs. In contrast, a homogeneous surface source distribution in purely elastic or acoustic cases does recover the correct phases of surface-wave modes (e.g. Snieder 2004; Halliday & Curtis 2008). However, correct amplitudes are not recovered in any of these cases. In practice, ambient seismic sources are typically more localized or azimuthally concentrated than spatially uniform (Ardhuin et al. 2015; Nakata et al. 2019). As a result, to achieve the level of accuracy required by FWI analysis, cross-correlated wavefields must be modelled as selfconsistent observations rather than as approximations of Green's functions.

Scholte

Scholte

Recognizing these limitations, Tromp et al. (2010) introduced a framework for modelling interstation cross-correlations that accounts for the distribution of ambient energy sources. This framework has been successfully used for inverting ambient source distributions and velocity structures in global seismology (Ermert et al. 2017; Sager et al. 2018), particularly for the primary microseism frequency band (i.e. sub-0.1 Hz), where sources can be approximated as acting at the ocean bottom and the effect of the water column can be neglected (Longuet-Higgins 1950; Nakata et al. 2019). However, this framework is limited to elastic systems and models the ocean layer as a surface load (Komatitsch & Tromp 2002b). This simplification reduces its effectiveness in modelling and interpreting exploration-scale ambient ocean-bottom sensor cross-correlation wavefields in the secondary microseism frequency band (0.1-1.0 Hz) where sources are distributed as pressure fluctuations at or near the ocean surface and the effects of ocean depth cannot be neglected (Longuet-Higgins 1950; Hasselmann 1963; Ardhuin & Herbers 2013; Nakata et al. 2019). To accurately model secondary microseism cross-correlations recorded on oceanbottom sensors and to evaluate how marine physical properties affect VSG data, we require cross-correlation representations in a coupled

acoustic-elastic systems with a fluid-solid interface, characteristic of ocean-bottom seismology

To address these challenges, Pandey et al. (2025) presents comprehensive derivations and examples of Green's function representations for ocean-bottom seismic interferometry in coupled acoustic—elastic media. However, these representations require ambient source distributions and types that are not typically available in practical scenarios. The study shows that inter-receiver cross-correlations recorded on dense OBS arrays, when subjected to realistic ambient source distributions, fail to recover the correct phase and amplitude of the inter-receiver surface wave Green's function. This limitation renders the presented Green's function representations ineffective for investigating realistic ambient source distributions in ocean settings.

The objective of this study is twofold: (1) to outline a comprehensive framework for modelling pressure and (particle) velocity cross-correlated wavefields for dense ocean-bottom sensor array under different ambient source types and spatial distributions within a coupled acoustic-elastic system; and (2) to investigate the complementary effects of key first-order physical control factors ocean-bottom velocity structures, ambient energy source locations, ocean-bottom bathymetric depth and variations and inhomogeneous ambient energy source distributions—on the excitation and energy partitioning of surface- and body-wave modes recorded on oceanbottom sensors. OBN data potentially allow for 16 cross-component correlations derived from pressure and three-component particle velocity recordings. However, to avoid cross-correlating velocity and pressure quantities as they have different physical meanings, we only model and analyse the pressure-to-pressure and  $3 \times 3$  particlevelocity VSG tensor cross-correlations, incorporating both flat and variable bathymetry with homogeneous and heterogeneous ambient source distributions. Specifically, we address the following questions: (1) How does the spatial distribution of ambient sources affect surface- and body-wave excitation? (2) How does oceanbottom depth influence the excitation and energy partitioning of these wave modes? (3) Are all cross-correlation components equally significant and, if not, which cross-correlation components best capture different wave modes? and (4) What conditions are necessary for Love-wave generation and how do inhomogeneous ambient source distributions affect their detectability? Finally, we discuss the observations made during the investigation of these control factors in the context of the broader goal of using ambient seismic wavefield energy for long-wavelength structural imaging and elastic velocity model building in seismic exploration.

# 2 MODELLING AMBIENT VIRTUAL SHOT GATHERS FOR OCEAN-BOTTOM SENSORS

A key goal of most ambient seismic interferometry investigations is to use a cross-correlation methodology to recover accurate estimates of the Green's function between pairs of observation points. However, numerous experimental factors, such as the unavailability of favourable source types and distributions, commonly prevent VSG observations from accurately representing Green's functions. Herein, we choose not to rely on Green's function retrieval assumptions and instead interpret ambient cross-correlations as self-consistent observables termed 'cross-correlation functions' (CCFs). Because this approach represents a departure from standard practice, we present a comprehensive derivation of the time-domain equations for modelling CCFs between ocean-bottom receiver pairs.

The CCF modelling methodology is derived from Tromp *et al.* (2010) and the work presented here extends this approach to modelling cross-correlation for ocean-bottom sensors located at the ocean-bottom coupled acoustic—elastic interface. We refer this framework as 'cross-correlation modelling' (CCM).

A continuous velocity CCF tensor, denoted  $C_{ij}$ , of two ambient wavefield recordings  $v_i$  and  $v_j$  at respective receiver locations  $\mathbf{x}_A = [x_1, x_2, x_3]_A$  and  $\mathbf{x}_B = [x_1, x_2, x_3]_B$  is explicitly given by

$$C_{ij}(\mathbf{x}_{A}, \mathbf{x}_{B}, \tau) = \int_{-T}^{T} v_{i}(\mathbf{x}_{A}, t) \cdot v_{j}(\mathbf{x}_{B}, t + \tau) dt$$
$$= v_{i}(\mathbf{x}_{A}, -t) * v_{j}(\mathbf{x}_{B}, t),$$
(1)

where  $\mathbf{x}_A$  denotes the main receiver or virtual shot point location at which cross-correlation is performed;  $\mathbf{x}_B$  represents the VSG receiver locations; T is the selected correlation window duration;  $v_i$  and  $v_j$  are the i and j components of the particle velocity vector recorded at receivers  $\mathbf{x}_A$  and  $\mathbf{x}_B$ ; t and  $\tau$  denote time and the temporal correlation lag; and \* represents the temporal convolution operator. Throughout the text, lowercase Latin subscripts take values of 1, 2, 3 and  $\mathbf{x} = [x_1, x_2, x_3]$  denotes a Cartesian coordinate vector with the  $x_3$ -axis oriented positive downwards.

Marine ambient sources typically act either as distributed pressure sources at the ocean surface or as point force sources localized at the seafloor bathymetry (e.g. Longuet-Higgins 1950; Hasselmann 1963; Nakata *et al.* 2019). We first derive the CCF expression for ambient pressure-type sources acting above the ocean bottom within the ocean's acoustic layer. We subsequently extend the analysis to include CCF expressions for force-type ambient sources acting below the ocean bottom within the underlying elastic solid.

A velocity wavefield  $v_i$  excited by the ambient pressure-type source signal N and observed at  $\mathbf{x}$  can be expressed through the velocity Green's function (Aki & Richards 2002) as

$$v_i(\mathbf{x}, t) = \int \left[ G_i^{v,q}(\mathbf{x}, \boldsymbol{\xi}, t') * N(\boldsymbol{\xi}, t') \right](t) \, \mathrm{d}\boldsymbol{\xi}, \tag{2}$$

where  $G_i^{v,q}(\mathbf{x}, \boldsymbol{\xi}, t')$  represents the i component of observed particle velocity v at  $\mathbf{x}$  due to an impulsive point pressure-type source q acting at spatial location  $\boldsymbol{\xi}$ ; and  $N(\boldsymbol{\xi}, t')$  denotes the ambient pressure-type source signal as a function of location  $\boldsymbol{\xi}$  and time t'. Convolution of time-reversed wavefields  $v_i(\mathbf{x}_A, -t)$  with  $v_j(\mathbf{x}_B, t)$  (eq. 1) results in the time-domain velocity CCF tensor component

$$C_{ij}(\mathbf{x}_{A}, \mathbf{x}_{B}) = \iint \left\{ \left[ G_{i}^{v,q}(\mathbf{x}_{A}, \boldsymbol{\xi}_{1}) * N(\boldsymbol{\xi}_{1}) \right] (-t) \right.$$

$$\left. * \left[ G_{i}^{v,q}(\mathbf{x}_{B}, \boldsymbol{\xi}_{2}) * N(\boldsymbol{\xi}_{2}) \right] (t) \right\} d\boldsymbol{\xi}_{1} d\boldsymbol{\xi}_{2}. \tag{3}$$

Note that here and below, the temporal lag  $\tau$  dependence is omitted from the expression for brevity. Rearranging the convolution in the above equation leads to

$$C_{ij}(\mathbf{x}_{A}, \mathbf{x}_{B}) = \iint \left[ G_{j}^{v,q}(\mathbf{x}_{B}, \boldsymbol{\xi}_{2}, t) * G_{i}^{v,q}(\mathbf{x}_{A}, \boldsymbol{\xi}_{1}, -t) \right] * \left[ N(\boldsymbol{\xi}_{1}, -t) * N(\boldsymbol{\xi}_{2}, t) \right] d\boldsymbol{\xi}_{1} d\boldsymbol{\xi}_{2}.$$
(4)

Usually, traces are correlated over a selected time range for a large number of windowed subsets of the long-time recording and subsequently stacked, which effectively amounts to computing the expected value of the CCF tensor component. Therefore, we determine the ensemble-averaged velocity CCF given by

$$\langle \mathcal{C}_{ij}(\mathbf{x}_{\mathbf{A}}, \mathbf{x}_{\mathbf{B}}) \rangle = \iint \left[ G_j^{v,q}(\mathbf{x}_{\mathbf{B}}, \boldsymbol{\xi}_2, t) * G_i^{v,q}(\mathbf{x}_{\mathbf{A}}, \boldsymbol{\xi}_1, -t) \right] * \langle \left[ N(\boldsymbol{\xi}_1, -t) * N(\boldsymbol{\xi}_2, t) \right] \rangle d\boldsymbol{\xi}_1 d\boldsymbol{\xi}_2,$$
 (5)

where  $\langle \cdot \rangle$  denotes an ensemble average. In practical applications, it is often assumed that ambient sources are mutually uncorrelated (e.g. Weaver & Lobkis 2001; Snieder 2004; Shapiro *et al.* 2005; Wapenaar & Fokkema 2006) and the ambient source spectra for all sources  $N(\xi,t)$  are similar (e.g. Ermert *et al.* 2017; Xu *et al.* 2019) such that

$$\langle N(\boldsymbol{\xi}_1, -t) * N(\boldsymbol{\xi}_2, t) \rangle = S(\boldsymbol{\xi}, t) \, \delta(\boldsymbol{\xi} - \boldsymbol{\xi}_1) \, \delta(\boldsymbol{\xi} - \boldsymbol{\xi}_2), \tag{6}$$

where  $\delta(\xi)$  is a 2-D spatial delta function, and  $S(\xi, t)$  is ambient pressure-source autocorrelation function. This assumption simplifies eq. (5) to

$$\langle \mathcal{C}_{ij}(\mathbf{x}_{A}, \mathbf{x}_{B}) \rangle = \int G_{j}^{v,q}(\mathbf{x}_{B}, \boldsymbol{\xi}, t) * \left[ G_{i}^{v,q}(\mathbf{x}_{A}, \boldsymbol{\xi}, -t) * S(\boldsymbol{\xi}, t) \right] d\boldsymbol{\xi}.$$
(7)

Using the source-receiver reciprocity relationship in a coupled acoustic-over-elastic system, where a receiver at  $\xi$  in the acoustic medium records pressure p due to a point force source f in the i-th direction at  $\mathbf{x}_A$  in the elastic medium (right-hand term in the equation below), and conversely, a receiver at  $\mathbf{x}_A$  records the i-th component of particle velocity v due to a pressure-type source q at  $\xi$  (left-hand term in the equation below) (Pandey et al. 2025),

$$G_i^{v,q}(\mathbf{x}_{\mathcal{A}}, \boldsymbol{\xi}, t) = -G_{i}^{p,f}(\boldsymbol{\xi}, \mathbf{x}_{\mathcal{A}}, t), \tag{8}$$

we can rewrite eq. (7) as

$$\langle \mathcal{C}_{ij}(\mathbf{x}_{A}, \mathbf{x}_{B}) \rangle = -\int G_{j}^{v,q}(\mathbf{x}_{B}, \boldsymbol{\xi}, t) * \left[ G_{,i}^{p,f}(\boldsymbol{\xi}, \mathbf{x}_{A}, -t) * S(\boldsymbol{\xi}, t) \right] d\boldsymbol{\xi}.$$
 (9)

The coupled source–receiver reciprocity relation given in eq. (8) is derived in Pandey *et al.* (2025). The negative sign is a result of the coupling between the acoustic and elastic systems through the constitutive equations detailed in Pandey *et al.* (2025).

For a narrow frequency band (e.g. 0.05-1.0 Hz), we partition the ambient energy source function  $S(\xi, t)$  into its spatial and temporal dependences as

$$S(\xi, t) = S(\xi)S(t), \tag{10}$$

where the relative spatial distribution of ambient wavefield energy is defined such that  $S(\xi) = 0$  and  $S(\xi) = 1$  represent effective sources with zero and the highest energy at location  $\xi$ , respectively, and S(t) denotes the ambient source-time autocorrelation function. With these definitions, the time-averaged velocity CCF tensor of eq. (9) becomes

$$\langle \mathcal{C}_{ij}(\mathbf{x}_{\mathrm{A}}, \mathbf{x}_{\mathrm{B}}) \rangle = -\int G_{j}^{v,q}(\mathbf{x}_{\mathrm{B}}, \boldsymbol{\xi}, t) * \left\{ \left( G_{,i}^{p,f}(\boldsymbol{\xi}, \mathbf{x}_{\mathrm{A}}, -t) S(\boldsymbol{\xi}) \right) * S(t) \right\} d\boldsymbol{\xi}.$$
(11)

Comparing this result with eq. (2), we can now define the driving source (Tromp *et al.* 2010) of the ensemble CCF  $\langle C_{ij} \rangle$  as

$$q(\boldsymbol{\xi}, \mathbf{x}_{A}, t) = \left(G_{,i}^{p,f}(\boldsymbol{\xi}, \mathbf{x}_{A}, -t)S(\boldsymbol{\xi})\right) * S(t), \tag{12}$$

where q represents the pressure-type source injection. Thus, the driving source is simply the source-energy-weighted time-reversed wavefield recorded at ambient energy locations  $\xi$  due to a source with source-time function S(t) at the virtual shot point locations  $\mathbf{x}_A$ . Velocity CCF tensor components  $\langle \mathcal{C}_{ij} \rangle$  are the ensemble-averaged velocity wavefield recorded on ocean-bottom observation locations  $\mathbf{x}_B$  due to driving source q at  $\mathbf{x}_A$ .

For ambient sources acting as point forces on local bathymetry or within elastic solid, a similar expression for  $\langle C_{ij} \rangle$  can be written:

$$\langle \mathcal{C}_{ij}(\mathbf{x}_{\mathrm{A}}, \mathbf{x}_{\mathrm{B}}) \rangle = \int G_{j,n}^{v,f}(\mathbf{x}_{\mathrm{B}}, \boldsymbol{\xi}, t) * \left\{ \left( G_{n,i}^{v,f}(\boldsymbol{\xi}, \mathbf{x}_{\mathrm{A}}, -t) S(\boldsymbol{\xi}) \right) * S(t) \right\} d\boldsymbol{\xi}. \tag{13}$$

Similar to the case of pressure-type ambient sources, the above equation assumes that two ambient force sources—one acting in the n-direction at  $\xi_1$  and the other in the m-direction at  $\xi_2$ —are uncorrelated and share common spectra, that is,

$$\langle N_n(\boldsymbol{\xi}_1, -t) * N_m(\boldsymbol{\xi}_2, t) \rangle = S_{nm}(\boldsymbol{\xi}, t) \, \delta(\boldsymbol{\xi} - \boldsymbol{\xi}_1) \, \delta(\boldsymbol{\xi} - \boldsymbol{\xi}_2) \,, \tag{14}$$

where  $S_{nm}(\xi, t)$  is the force source autocorrelation function, which simplifies to  $S_{nm}(\xi, t) = S(\xi) S(t) \delta_{nm}$  for a narrow frequency band. Here,  $S(\xi)$  and S(t) have the same definitions as in the pressure case, but correspond to an ambient force source. Eq. (13) follows from applying elastic domain source–receiver reciprocity (Wapenaar & Fokkema 2006)

$$G_{i,n}^{v,f}(\mathbf{x}_{A}, \boldsymbol{\xi}, t) = G_{n,i}^{v,f}(\boldsymbol{\xi}, \mathbf{x}_{A}, t). \tag{15}$$

Note that in all instances of repeated subscripts in this paper, the summation convention applies. This implies that the right-hand side term in eq. (13) must be computed for n = 1, 2, 3 to account for all ambient force components when evaluating  $\langle C_{ij} \rangle$ :

$$\langle C_{ij}(\mathbf{x}_{A}, \mathbf{x}_{B}) \rangle = \int G_{j,1}^{v,f}(\mathbf{x}_{B}, \boldsymbol{\xi}, t) * \left\{ \left( G_{1,i}^{v,f}(\boldsymbol{\xi}, \mathbf{x}_{A}, -t) S(\boldsymbol{\xi}) \right) * S(t) \right\} d\boldsymbol{\xi}$$

$$+ \int G_{j,2}^{v,f}(\mathbf{x}_{B}, \boldsymbol{\xi}, t) * \left\{ \left( G_{2,i}^{v,f}(\boldsymbol{\xi}, \mathbf{x}_{A}, -t) S(\boldsymbol{\xi}) \right) * S(t) \right\} d\boldsymbol{\xi}$$

$$+ \int G_{j,3}^{v,f}(\mathbf{x}_{B}, \boldsymbol{\xi}, t) * \left\{ \left( G_{3,i}^{v,f}(\boldsymbol{\xi}, \mathbf{x}_{A}, -t) S(\boldsymbol{\xi}) \right) * S(t) \right\} d\boldsymbol{\xi}.$$
 (16)

For pressure CCFs, represented as a scalar quantity C, and due to ambient force sources, an expression analogous to eq. (13) can be written using the coupled source–receiver reciprocity of eq. (8) as

$$\langle \mathcal{C}(\mathbf{x}_{A}, \mathbf{x}_{B}) \rangle = -\int G_{,n}^{p,f}(\mathbf{x}_{B}, \boldsymbol{\xi}, t) * \{ (G_{n}^{v,q}(\boldsymbol{\xi}, \mathbf{x}_{A}, -t)S(\boldsymbol{\xi})) * S(t) \} d\boldsymbol{\xi},$$
(17)

and for ambient pressure sources, an expression similar to eq. (11) can be written using the acoustic-domain source–receiver reciprocity (Wapenaar & Fokkema 2006):

$$G^{p,q}(\mathbf{x}_{A}, \boldsymbol{\xi}, t) = G^{p,q}(\boldsymbol{\xi}, \mathbf{x}_{A}, t), \tag{18}$$

as

$$\langle \mathcal{C}(\mathbf{x}_{A}, \mathbf{x}_{B}) \rangle = \int G^{p,q}(\mathbf{x}_{B}, \boldsymbol{\xi}, t) * \{ (G^{p,q}(\boldsymbol{\xi}, \mathbf{x}_{A}, -t)S(\boldsymbol{\xi})) * S(t) \} d\boldsymbol{\xi}.$$
 (19)

Eqs (11), (13), (17) and (19) provide the basis for the forward modelling of all velocity and pressure CCFs for dense ocean-bottom sensor arrays for different ambient source types, locations and configurations. When CCFs are assembled for multiple receivers relative to a main receiver acting as a virtual shot point, the resulting gather is referred to as a VSG.

### 2.1.1 Ambient CCFs forward modelling workflow

Modelling ensemble cross-correlation functions under the CCM framework differs from active-shot modelling in exploration seismology because it requires two passes of forward 3-D elastic wave propagation for each ambient sources component. The first pass computes the driving source (eq. 12), which depends on the ambient source-energy distribution  $S(\xi)$  and the ambient wavefield source-time autocorrelation function S(t). The distribution  $S(\xi)$  can be estimated using real data through back-projection or beamforming techniques, while S(t) is a zero-phase wavelet with a duration equal to the simulation time or 2n-1 time steps, where n represents the number of causal time steps. The magnitude spectrum of S(t)

corresponds to the ensemble-averaged power spectrum of ambient sources. The second pass evaluates the ensemble CCFs  $\langle C_{i,j} \rangle$  or  $\langle C \rangle$  (eqs 11, 13, 17 or 19) resulting from the driving source calculated during the first forward pass.

We model a velocity-component VSG for receivers located beneath the seafloor with a virtual shot point located at  $\mathbf{x}_A = [x_1, x_1, x_3]$  and for ambient sources acting as pressure sources on the ocean surface (eq. 11) using a numerically coupled acousticelastic wave propagation solver by performing the following steps:

- (i) Characterize the spatial distribution of the ensemble-averaged ambient wavefield energy  $S(\xi)$ .
- (ii) For i = 1, 2, or 3 velocity component, inject a force source with the source-time function S(t) in the i direction at the virtual shot point location  $\mathbf{x}_A$ .
- (iii) Record the pressure-component wavefield at ambient source locations  $\xi$  due to the source implemented in Step 2 (see  $G_i^{p,f}(\xi, \mathbf{x}_A, -t)$  in eq. 11).
- (iv) Time-reverse the recorded pressure wavefield and scale it by the ensemble-averaged ambient wavefield energy  $S(\xi)$  to generate the corresponding driving source q needed to model the ensemble CCFs.
- (v) Inject explosive sources at ambient source locations  $\xi$  with the source-time function as q. Sample the velocity wavefield components (i.e. particle velocity in j=1,2, or 3 directions) at other OBN locations  $\mathbf{x}_{\mathrm{B}}$ , and multiply by -1 to compute the desired CCFs.

If using i=3 in Step 2 (i.e. injecting a vertical force source) and sampling the j=3 component of the velocity wavefield in Step 5, the modelled CCFs would correspond to a vertical–vertical autocomponent velocity VSG  $\langle \mathcal{C}_{33} \rangle$ . Similarly, if using i=1 in Step 2 (i.e. injecting a horizontal force source) and sampling the j=2 component of the velocity wavefield in Step 5, the modelled CCFs would correspond to a horizontal–horizontal cross-component VSG  $\langle \mathcal{C}_{12} \rangle$ . The modelling equations for generating velocity CCFs due to ambient force sources (eq. 13) and pressure CCFs (eqs 17 and 19) are implemented through similar workflows.

In the following sections, for clarity and intuitiveness, we switch from the Cartesian coordinate vector notation  $\mathbf{x} = [x_1, x_2, x_3]$  to  $\mathbf{x} = [x, y, z]$  or [r, t, v]. Here, x points East, y points North and z is oriented positive downwards. The symbols r and t represent the radial and transverse directions in the x-y plane, while v corresponds to the vertical direction z. We previously avoided this notation because Latin subscripts were used generically to imply summation over repeated indices, whereas x, y and z refer to fixed coordinate axes.

### 3 NUMERICAL EXPERIMENTS

We now simulate the low-frequency vertical-component velocity cross-correlation wavefield recorded on ocean-bottom sensors using CCM approach for different offshore Earth model scenarios. We begin with a flat seafloor and 1-D  $v_p(z)$  and  $v_s(z)$  velocity profiles beneath the ocean bottom. To study the different wave modes in the modelled cross-correlation wavefields and the associated dispersion characteristics, we use two groups of ocean-bottom velocity models: (1) a soft bottom (SB) with  $v_s$  at the seafloor being much slower than the acoustic fluid velocity  $v_f$ ; and (2) a hard bottom (HB) with  $v_s$  at the seafloor slightly faster than  $v_f$ . Table 2 presents the

ocean-bottom model elastic properties where the  $v_p$ ,  $v_s$  and  $\rho$  are defined at the ocean bottom and increase with depth according to the listed velocity gradients. Physical properties remain constant below 11 km beneath the ocean bottom. The acoustic velocity,  $v_f$ , and density,  $\rho_f$ , of the homogeneous water layer are respectively set to 1500 m s<sup>-1</sup> and 1000 kg m<sup>-3</sup>. Seismic attenuation is not considered, as attenuation properties at these frequencies are largely unknown. We simulate forward wave propagation using SPECFEM3D Cartesian 4.1.0 (Komatitsch & Tromp 2002a, b; Komatitsch et al. 2023) published under the GPL3 license. The open-source software implements the 3-D spectral element method (Komatitsch et al. 2000) for wave-propagation modelling. We note throughout that: (1) only the causal part of VSGs and their associated dispersion spectra of phase velocities—herein referred to as dispersion panels—are plotted; and (2) the relative amplitudes between VSGs are not preserved. However, a scale factor relative to the vertical-vertical velocity CCF,  $C_{vv}$ , is indicated at the bottom of the plots where appropriate.

The extents of the synthetic 3-D models used in different sections of this paper are listed in Table 3. For flat ocean-bottom scenarios (Sections 3.1, 3.2 and 3.3.1), a regular grid spacing of 0.4 km  $\times$  0.4 km  $\times$  0.25 km (dx  $\times$  dy  $\times$  dz) is used. For the variable bathymetry models (Sections 3.3.2 and 3.4), the grid spacing in the x and y directions remains the same, while the spacing in the z-direction is adjusted to conform to the bathymetric profile. The ambient source-time autocorrelation function S(t) used in all simulations is a zero-phase Ricker wavelet with a 0.35 Hz central frequency. We use a free-surface top boundary with all other sides defined as absorbing boundary layers.

To estimate reliable dispersion curves, an interstation spacing of at least 3.0 wavelengths is needed (i.e.  $\Delta > 3\lambda$ ) (Bensen *et al.* 2007) or equivalently, a minimum reliable frequency  $f_{\min} = 3c/\Delta$ , where  $\Delta$  is the interstation spacing, c is the phase velocity and f is the frequency. For a maximum observed phase velocity of 3.0 km s<sup>-1</sup> and a maximum interstation spacing of 100 km with available measurements in our simulations, this results in a minimum reliable frequency of  $f_{\min} = 0.09$  Hz for our analysis. To compute the dispersion panels, we used an in-house C code that implements the phase-shift method (Park et al. 1999), which employs a phase coherency measure for surface-wave dispersion analysis. This code is adapted from the MATLAB implementation provided by Ólafsdóttir et al. (2018). Note that in the algorithm, Fourier transform is applied to each trace of the multichannel record providing its frequency-domain representation. Subsequently, the amplitude of the transformed record is normalized on the unit interval in both the offset and the frequency dimensions, with each panel normalized independently. Therefore, relative amplitudes between dispersion panels are not preserved.

## 3.1 Uniform ambient source distribution at different depths in ocean-water layer

At frequencies below 1.0 Hz, the observed ambient wavefield energy is primarily generated by ocean waves driven by two main mechanisms: (1) a primary microseism caused by the interference of ocean waves with bottom topography, which generates dominant energy in the 0.05–0.10 Hz range; and (2) a secondary microseism produced by the interference of pairs of ocean wave trains on the ocean surface, generating dominant energy in the 0.10–1.00 Hz frequency

Table 2. Model parameters of the SB and HB models.

Model	Ocean-bottom $P$ -wave velocity $v_p \text{ (m s}^{-1})$	Ocean-bottom S-wave velocity $v_s \text{ (m s}^{-1})$	Ocean-bottom Density $\rho \text{ (kg m}^{-3}\text{)}$	$v_p$ gradient below ocean bottom (km/s per km)	$v_s$ gradient below ocean bottom (km/s per km)
SB	1800	600	2100	0.40	0.23
HB	3400	1600	2100	0.40	0.23

Table 3. 3-D synthetic model settings used in different sections and corresponding figures.

Section	Model size (km) $x \times y \times z$	Source distribution	Ocean bottom	Figures and corresponding model
3.1	190 × 80 × 16.5	Homogeneous at depths: (a) 0.00 km, (b) 0.50 km, (c) 1.00 km, (d) 1.49 km	Flat at 1.50 km	Fig. 1 (SB), Fig. 2 (HB)
3.2	$190 \times 80 \times$	Homogeneous at surface	Flat at	Fig. 7 (SB),
	(a) 15.25, (b) 15.75,		(a) 0.25 km, (b) 0.75 km,	Fig. 8 (HB)
	(c) 16.50, (d) 17.25		(c) 1.50 km, (d) 2.25 km	
3.3.1	$200 \times 160 \times 16.5$	Homogeneous at surface	Flat at 0.75 km	Figs 10, 11, 12 (SB) Figs 13, 14, 15 (HB)
3.3.2	$160 \times 120 \times 16.5$	Inhomogeneous at surface	Variable bathymetry	Figs 17, 18, 19, 20 (SB) Figs 21, 22, 23 (HB)
3.4	$150\times150\times16.5$	Inhomogeneous at surface	Variable bathymetry	Fig. 24 (SB)

range (e.g. Longuet-Higgins 1950; Hasselmann 1963; Ardhuin & Herbers 2013). For the former, the seismic source can be described as a combination of tangential and vertical forces acting on the local bathymetry, while in the latter, the source is a distributed pressure field acting on or just below the ocean surface (Nakata *et al.* 2019). It should be noted that, because a Ricker wavelet with a 0.35 Hz central frequency is used in all simulations presented herein, some energy extends above 1.0 Hz and below 0.1 Hz. However, the dominant energy remains confined to the secondary microseism frequency band of 0.1–1.0 Hz.

To investigate the excitation of different wave modes and their characteristics arising from variations in the locations of ambient wavefield energy sources, we uniformly distributed ambient pressure-type sources at each grid point at four different depths within the ocean-water layer, treating each depth as a separate case. Table 3 presents the model settings. The ocean-bottom interface was held constant at 1.50 km depth, and the receivers were positioned just below the ocean bottom at 1.51 km depth at each grid point along the x-axis, forming a single line covering 100 km offset. The virtual shot point is located at one end of the array at  $[x_1, y_1, z_1] = [48.00, 40.00, 1.51]$  km.

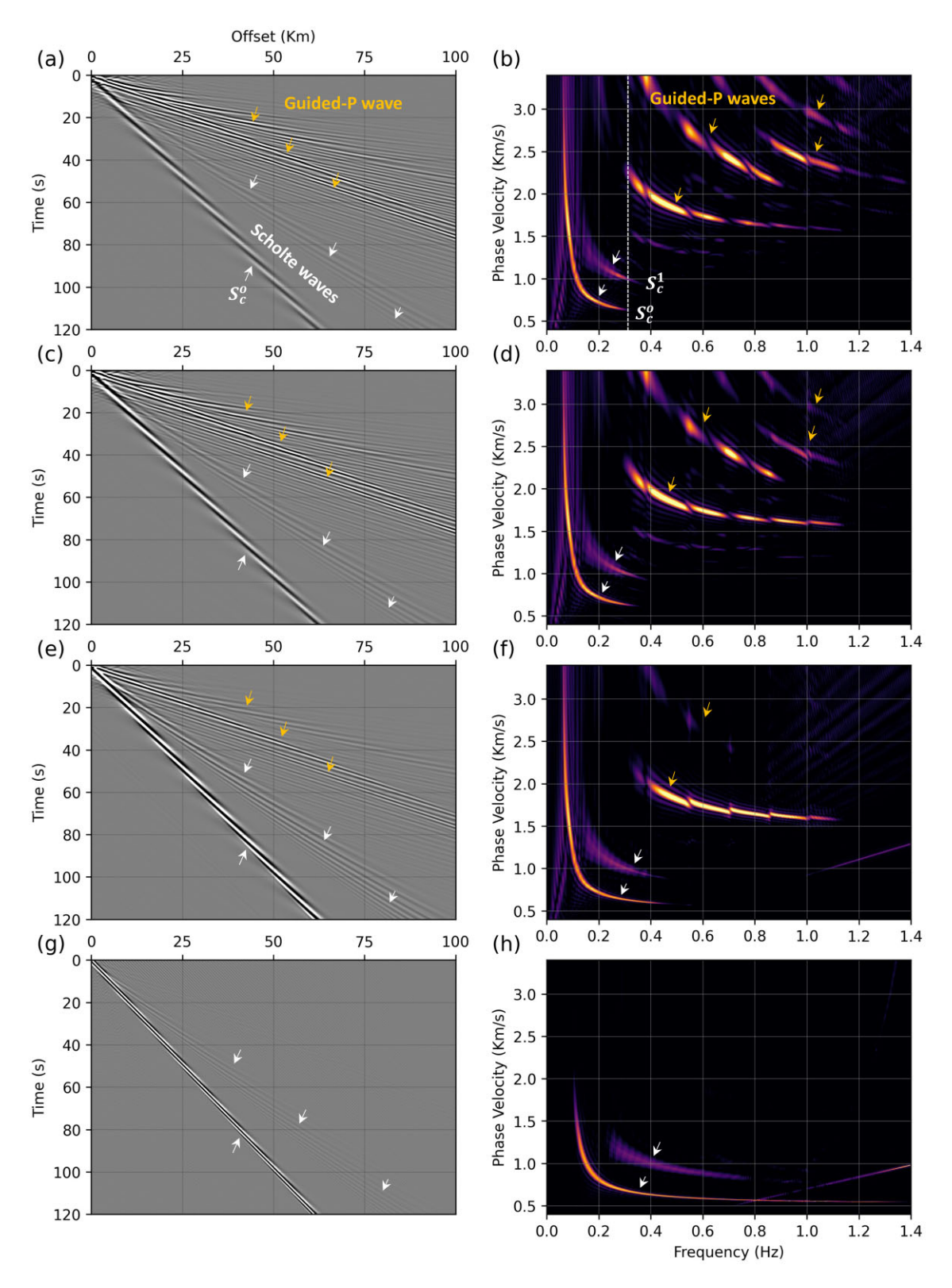
Figs 1 and 2 depict the VSGs (left column) and corresponding dispersion panels (right column) for the SB and HB model scenarios, respectively, with ambient energy sources at the following depths: (a,b) 0.00 km, (c,d) 0.50 km, (e,f) 1.00 km and (g,h) 1.49 km. Although ambient sources do not physically exist throughout the ocean column, placing them at different depths in a controlled modelling framework provides insight into the excitation of various wave modes and energy partitioning. Cases where sources are located near the ocean bottom (i.e. 1.49 km) are modelled as pressure sources with the full frequency band. However, in reality, such ambient sources are typically associated with primary microseisms and act as force sources on the seafloor.

From the SB and HB cases, respectively, shown in Figs 1 and 2, we observe two types of dispersive seismic waves in this marine setting: Scholte waves and guided P waves (also referred to as acoustic guided waves). These wave modes are identified with the help of theoretical P–SV wave dispersion curves, computed using the Computer Programs in Seismology package (Herrmann

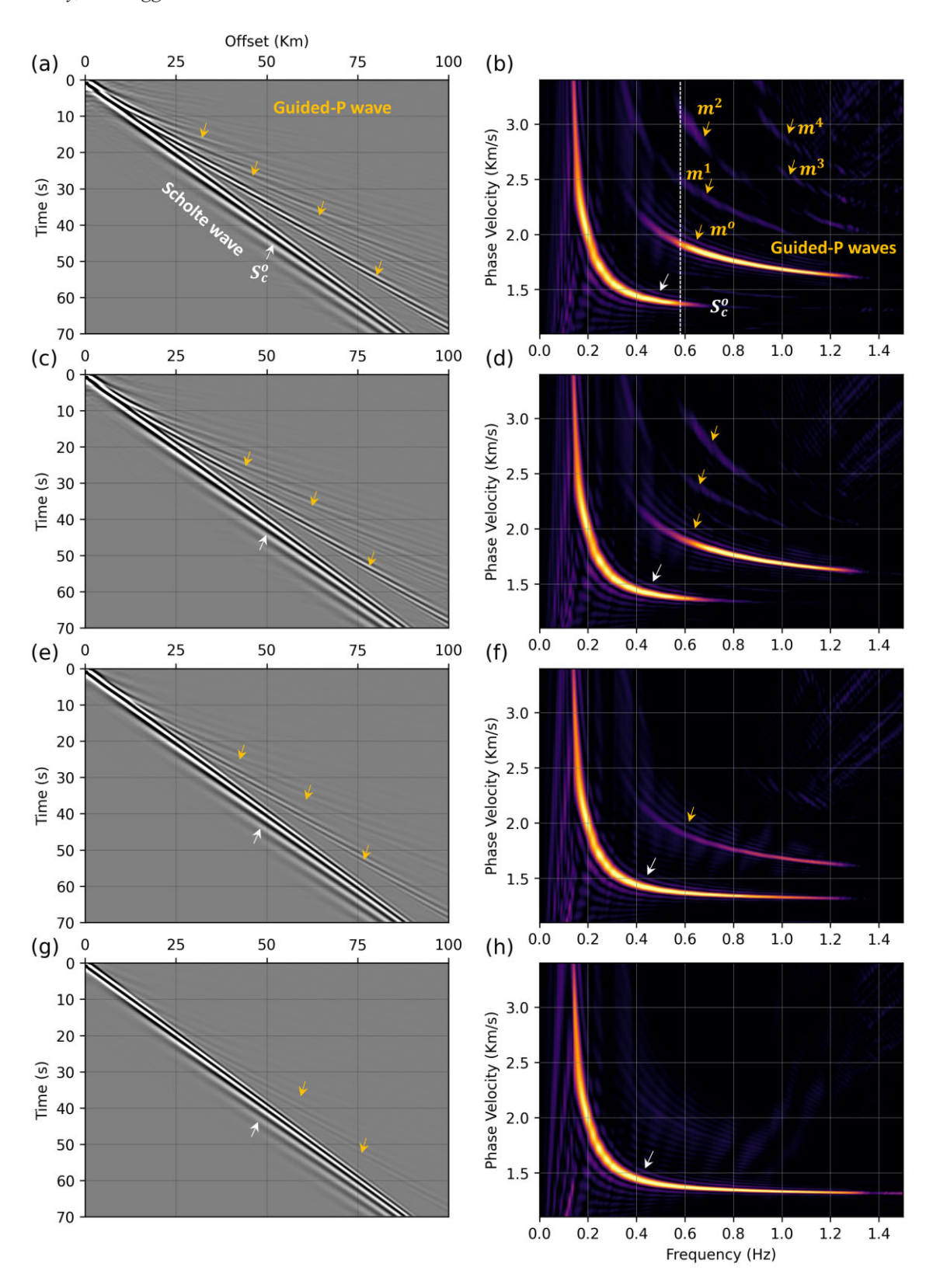
2013), and overlain on the calculated dispersion panels shown in Fig. 3.

Fig. 4 shows formation of Scholte and guided waves at oceanbottom from an airgun source. As described by Klein (2003) and Klein et al. (2005), both wave types are eigenmodes of wave propagation in a medium with purely depth-dependent properties. From a theoretical perspective, these wavefields correspond to solutions of the boundary value problem for the P-SV polarized seismic displacement field. Scholte-wave solutions exist only for a discrete set of real wavenumbers at a given real frequency. In contrast, guided P waves are characterized by complex-valued wavenumbers, where the real and imaginary components represent wave slowness (or phase velocity) and wave attenuation (i.e. energy leakage), respectively (e.g Aki & Richards 2002). Whether defined by real or complex wavenumbers, these waves are aligned along continuous dispersion curves in the frequency-phase velocity domain. Each dispersion curve corresponds to a distinct solution 'mode' (see Fig. 3). The observed wavefields can be interpreted in terms of physical characteristics such as phase velocity, mode number and group velocity, and identified as Scholte or guided P waves generally depending on the associated frequency and mode characteristics.

In the context of a marine setting, we refer to a wave as a guided P wave when its energy is concentrated within the water column and decays exponentially with depth into the underlying elastic medium. Physically, this wave type can be understood as the constructive interference of P-wave energy that is post-critically reflected and refracted at the seafloor, reverberating within the water layer or becoming trapped in shallow, unconsolidated ocean-bed sediments (Pekeris 1948; Klein et al. 2005). In Fig. 4, when the incident angle exceeds the critical angle  $\theta_c$  at the ocean bottom, total reflection and refraction occur and the resulting energy becomes confined within the waveguide formed by the free surface and the strong impedance discontinuity at the seafloor. After repeatedly bouncing between the top and bottom boundaries, these reflections and refractions superimpose and interfere to form guided P-waves. These waves exhibit frequency-dependent (dispersive) behaviour and possess phase velocities that exceed the acoustic velocity of water (Shtivelman 2004). Due to their relatively high amplitudes



**Figure 1.** Vertical-component VSGs (left column) with corresponding dispersion panels (right column) for the SB model (see Table 2) with a constant 1.50 km water depth. Ambient energy sources are uniformly distributed at the following depths within ocean-water layer: (a, b) 0.00 km, (c, d) 0.50 km, (e, f) 1.00 km and (g, h) 1.49 km. Scholte and guided *P*-wave modes are highlighted by white and yellow arrows, respectively. The vertical dotted line in panel (b) highlights the mode-truncation effect: the high-frequency band and the dispersive higher-mode energy of the Scholte waves are suppressed by the strong, dispersive guided *P* waves.



**Figure 2.** Vertical-component VSGs (left column) with corresponding dispersion panels (right column) for the HB model (see Table 2) with a constant 1.50 km water depth. Ambient energy sources are uniformly distributed at the following depths within ocean-water layer: (a, b) 0.00 km, (c, d) 0.50 km, (e, f) 1.00 km and (g, h) 1.49 km. Scholte and guided *P*-wave modes are highlighted by white and yellow arrows, respectively. The vertical dotted line in panel (b) highlights the mode-truncation effect.

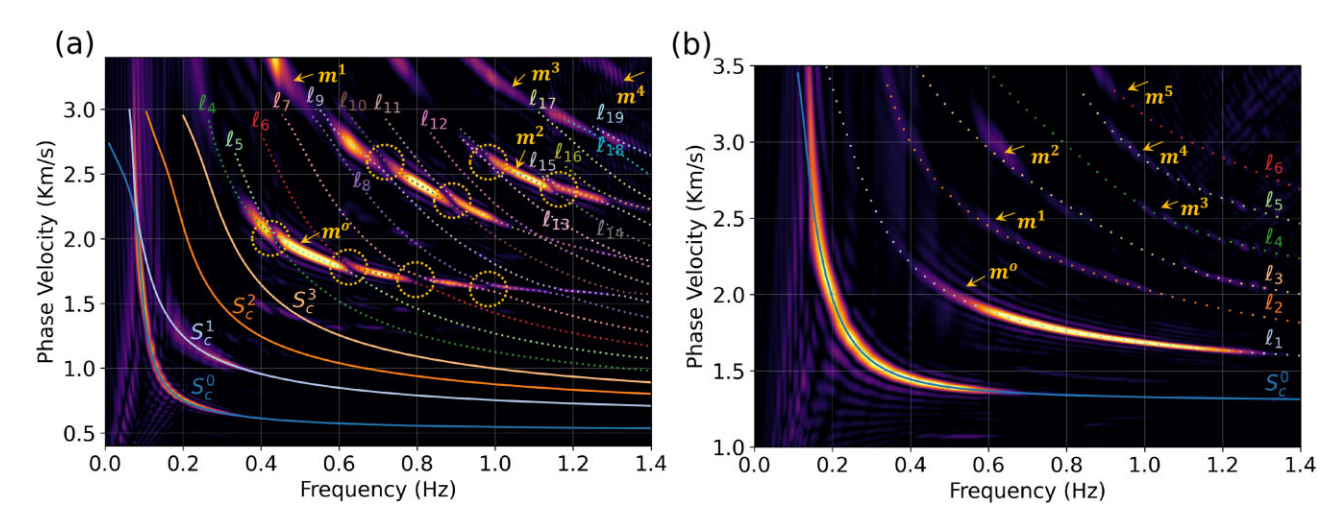


Figure 3. Theoretical complete P–SV wave dispersion curves overlaid on the dispersion panels for (a) the SB model case from Fig. 1(b) and (b) the HB model case from Fig. 2(b). Theoretical Scholte modes are labelled as  $S_c$  (solid curves) and leaky modes as  $\ell$  (dotted curves), with superscript  $^0$  denoting the fundamental mode and higher indices indicating higher-order modes. In panel (a), the mode kissing phenomenon (Sun *et al.* 2017) is highlighted with circles, following the trajectory of the guided P-wave dispersion energy, labelled as  $m^0 - m^4$ . In panel (b), the leaky modes follow the guided P-wave dispersion energy.

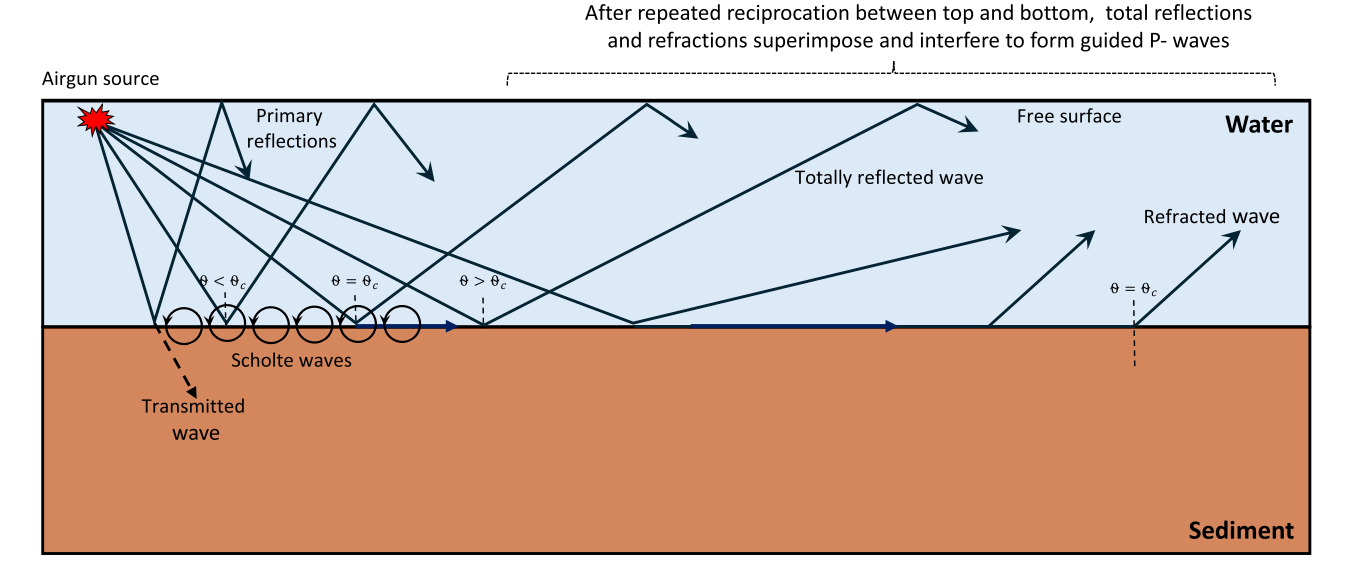


Figure 4. A schematic showing the formation of Scholte and guided P waves at the ocean bottom from an airgun source.

and efficient propagation within the waveguide with minimal energy loss, guided *P* waves can obscure surface-wave modes and deeper seismic reflections. However, they concentrate along the interface, interact with the seabed and are therefore sensitive to near-surface elastic properties and carry useful shallow subsurface information that cannot be obtained from the reflected and refracted wave (Klein *et al.* 2005; Sun *et al.* 2021; Kennett 2023; Gao *et al.* 2025).

In shallow marine environments, when the ocean depth d is small compared to the dominant seismic wavelength, the influence of the water layer on wave energy is minimal at low frequencies. However, at higher frequencies, the amplitudes of the P–SV polarized wavefield are greatest near the fluid–solid interface. Such waves,

commonly referred to as Scholte waves, propagate along the water-sediment interface in marine settings and are analogous to terrestrial Rayleigh waves (Scholte 1947). Scholte waves are highly dispersive and exhibit particle motion polarized in the vertical–radial (*P–SV*) plane. The transverse surface-wave component is known as a Love wave (Love 1911).

To address the distinction between Scholte and Rayleigh waves in the context of oceanic surface waves, we present in Figs 5 and 6. Herein, we refer to a *P*–*SV* polarized surface wave as a Scholte wave when its vertical displacement is concentrated near the fluid–solid interface (black curve in Fig. 5, and labelled Scholte in Fig. 6). These waves typically occur in the presence of thick oceanic sediments between the ocean bottom and the crust. In contrast, Rayleigh

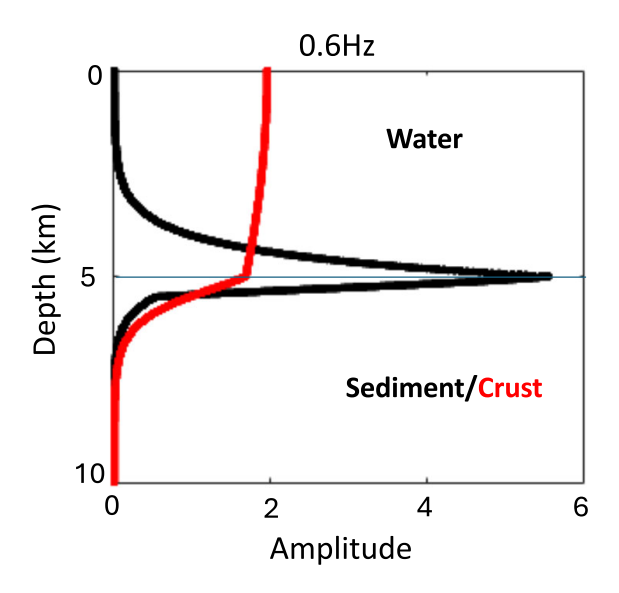


**Figure 5.** Vertical displacement eigenfunctions for fundamental mode Scholte/Rayleigh wave for a simple two-layer ocean model. For the black curve, the second layer is a sediment layer, and for the red curve, the second layer is a crustal layer. In our analysis, we refer to the black curve as representing Scholte waves, characterized by displacement concentrated at the water–sediment interface. The red curve corresponds to the water–crust model and is generally referred to as a Rayleigh wave in the literature, with vertical displacement more concentrated at the sea surface.

waves exhibit vertical displacement concentrated more at the sea surface (red curve in Figs 5) and typically arise when the crust lies directly beneath the ocean bottom or when the sediment thickness between the seabed and crust is negligible relative to the dominant wavelength. Therefore, in the presence of sediment between the seabed and the crust, the depth-dependent pattern of displacement and stress (i.e. the eigenfunction), or the transition from Rayleigh to Scholte wave behaviour, evolves not only with frequency but also with variations in water depth, sediment thickness and velocity structure (Ruan et al. 2014; Gualtieri et al. 2015; Xu et al. 2025). In all models presented in this study, sediments extend to approximately 12.0 km depth below the ocean bottom in the SB case and 8.0 km in the HB case before the P- and S-wave velocities reach crustal values (i.e. about 6.8 and 3.2 km s<sup>-1</sup>, respectively). Thus, the *P–SV* polarized surface wave mode we observe is referred to as a Scholte wave.

From Figs 1 and 2, we note that ambient energy sources located at or near the ocean surface (Figs 1a and 2a) generate the strongest dispersive guided P-wave amplitudes (yellow arrows) relative to dispersive Scholte waves (white arrows) in their corresponding panels. The number of observed guided P-wave modes (e.g.  $m^0 - m^4$  in Fig. 2b) decreases as the ambient energy sources approach the seabed as evident from the dispersion panels in Figs 1 and 2. When ambient energy sources are near the seabed, the guided P waves are nearly absent in the VSGs and corresponding dispersion panels (Figs 1g, h and 2g, h) because of the high efficiency of source-energy conversion to surface-wave modes.

The dispersion panels exhibit a clear truncation effect when guided P-wave modes are present: the high-frequency band and the high-mode dispersion energy of the Scholte wave modes are visually suppressed by the strong, dispersive guided P-wave modes. The higher Scholte modes are difficult to identify due to the strong dispersion energy of the guided P modes. The truncation

frequency—defined as the frequency around which energy transitions smoothly from the Scholte mode to the guided P-wave mode—is indicated by the white vertical lines in Figs 1(b) and 2(b). As guided P-wave modes decrease in number and amplitude with increasing source depth, the dispersion panels show that the fundamental Scholte wave mode ( $S_{\rm c}^0$ ) and its first overtone ( $S_{\rm c}^1$ ) exhibit a broader frequency bandwidth due to the reduced energy of strongly dispersive guided P modes. However, in cases where the Scholte wave modes are strongly truncated in the dispersion panels (e.g. Figs 1b and 1d), suppressing or muting the guided P waves prior to extracting the dispersion spectrum can extend the observable dispersive behaviour of the Scholte wave modes and increase their usable frequency range in the resulting dispersion panel.

## 3.2 Effect of ocean-water depth on Scholte and guided *P*-wave excitation from secondary microseism sources

To illustrate the effects of water depth on the partitioning of Scholte and guided *P*-wave energy recorded on ocean-bottom sensors from secondary microseism sources, we consider the SB and HB model properties of Table 2 with constant elastic layer thickness of 15 km but with different water depths and a flat seabed configuration. Table 3 presents the model settings. The ambient energy sources are uniformly distributed as pressure-type sources over the ocean surface at each grid point and the receivers are positioned 10 m below the ocean floor. Figs 7 and 8 show the vertical-component VSGs (left column) and associated dispersion panels (right column) for the SB and HB model scenarios, respectively, with ocean-water depths of: (a, b) 0.25 km, (c, d) 0.75 km, (e, f) 1.50 km and (g, h) 2.25 km.

From the dispersion panels presented in Figs 7 and 8, we observe that the guided *P*-wave energy (yellow arrows) becomes increasingly dominant with increasing water depth, extending further into the lower-frequency range. This results in the truncation of the high-frequency end and the suppression of higher-order Scholte wave modes (white arrows), thereby narrowing the Scholte-wave frequency band. Furthermore, as the water depth increases, a progressively greater portion of the source energy transitions to guided *P*-wave modes, leading to a significant weakening of Scholte wave modes (see Figs 7 and 8 VSGs).

As illustrated from VSGs in Figs 7(g) and 8(g) for the SB and HB models, respectively, the fundamental Scholte mode,  $S_{\rm c}^0$ , weakens significantly with increasing depths. The corresponding dispersion panels in Figs 7(h) and 8(h) show that this mode exhibits a much narrower frequency bandwidth at deeper ocean bottoms. Specifically, in the SB model, the bandwidth reduces to below 0.2 Hz, while in the HB model, it falls below 0.4 Hz at a depth of 2.25 km. This narrowing contrasts with the broader bandwidth observed at shallower depths of 0.25 km as shown in Figs 7(b) and 8(b).

The results presented in Figs 7 and 8 suggest a complex interplay between ocean-bottom depth and the source frequencies in controlling the expressions of Scholte and guided P-wave modes. Specifically, when the ocean depth, d is small compared to the seismic wavelength,  $\lambda$  (e.g. Figs 7a, b and 8a, b), the entire acousticelastic system behaves as a single elastic system, as the effect of the water layer becomes negligible at such low source frequencies. Under these conditions (i.e.  $d << \lambda$ ), the influence of the ocean layer on seismic wave propagation can be accounted for as a load (Komatitsch & Tromp 2002b), and the Scholte

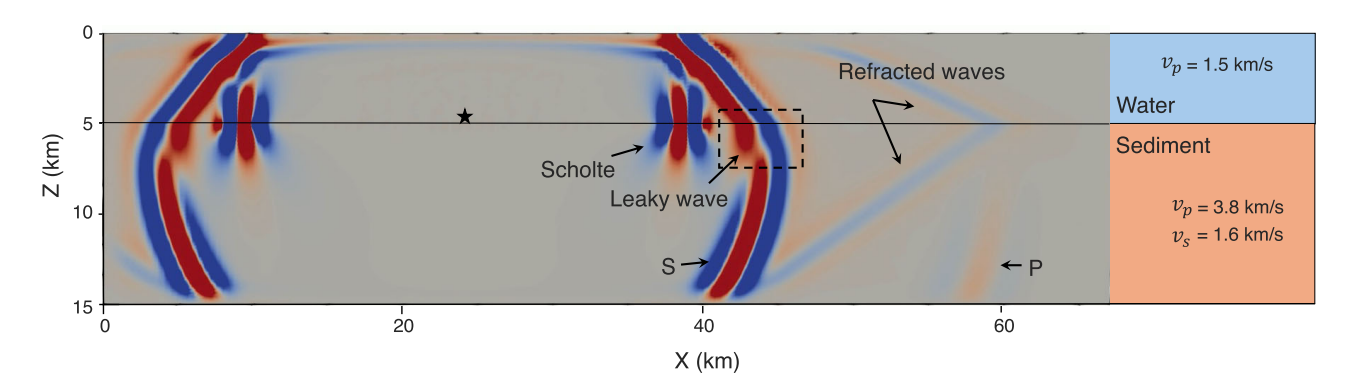


Figure 6. Surface and body wave modes in a water—homogeneous elastic half-space model excited by a low-frequency (0.6 Hz Ricker) source located just above the water—solid interface (indicated by a star). The surface wave mode is a Scholte wave, with displacement concentrated along the water—sediment boundary.

wave velocities tend to approach those of the Rayleigh wave determined by the sub-bottom elastic layer properties (Abrahams *et al.* 2023). In this scenario, a Scholte wave can be regarded as a Rayleigh wave (Klein 2003; Bohlen *et al.* 2004). Guided *P*-wave modes are either absent or are only weakly excited in this scenario.

When the ocean depth is large compared to the seismic wavelength (i.e.  $d >> \lambda$ ), though, this approximation no longer holds (e.g. Figs 7c-h and 8c-h). The propagation of P waves within the water layer exerts a non-negligible effect on other wave modes and has a dominant effect on the pressure field throughout the ocean (Longuet-Higgins 1950). In this scenario, the sources of secondary microseisms are located at or just below the ocean surface. The P waves generated at these source locations are multiply reflected between the ocean surface and the seafloor forming guided P waves, causing energy partitioning and truncation of Scholte-wave energy, as observed in the above examples.

### 3.3 Cross-correlation tensor components and bathymetric effects

The previous sections examined the modal content of vertical-vertical component CCFs to illustrate the effects of bathymetry and ambient source distributions. However, horizontal-horizontal and horizontal-vertical component CCFs also can provide relevant and equally valuable information not captured by vertical-vertical component CCFs. Accordingly, we now perform simulations to model the auto- and cross-component velocity VSGs, forming a 3 × 3 VSG tensor and a pressure–pressure component VSG. These simulations similarly assume uniform pressure-like sources at the ocean surface with source-time function as a Ricker wavelet of 0.35 Hz central frequency, accounting for interactions between oceanic waves at the ocean surface in the secondary microseism frequency band. We investigate the role of variable bathymetry and 3-D Earth structure in generating different wave modes, specifically focusing on Love-wave energy.

Because it is challenging to assess the polarization patterns of different wave modes in a Cartesian coordinate system defined by x, y and z components—due to the azimuthal dependence of radiation polarization pattern for the horizontal components—we reorient the recordings to radial (r), transverse (t) and vertical components (v) in a virtual-source-centric cylindrical coordinate system. For a receiver line oriented along the x-axis (see Fig. 9), the

x-direction becomes the radial direction, while the y-direction becomes the transverse direction. This nomenclature aligns the wave modes with the azimuth between each virtual source and receiver pair, allowing for a more natural representation of VSGs in terms of Love waves, as well as fundamental and higher-order Scholte waves. Note that in cases with bathymetric variations, such as in Section 3.3.2, the radial and transverse directions remain horizontal (i.e. in x-y plane), and the v-component remains aligned with z. The radial and transverse directions are not necessarily aligned parallel to, and the vertical direction perpendicular to, the local bathymetric gradient.

### 3.3.1 Flat ocean-bottom bathymetry and 3-D model with 1-D velocity structure

We first model a flat seafloor at 0.75 km depth and simulate results for 3-D SB and HB Earth models with the 1-D velocity structure (i.e. a v(z) velocity gradient) as detailed in Table 2. The lateral velocities do not change. Fig. 9(a) shows the geometry of the secondary microseism sources, OBNs, and location of virtual shot point. The pressure-type sources are uniformly distributed over the ocean surface. Table 3 presents the model settings. Given the assumptions of a flat seafloor and an isotropic source distribution relative to the receiver line, the velocity VSG tensor will be symmetric; thus, we present only the lower triangular elements of the matrix.

Fig. 10 shows the velocity VSG tensor components, while their corresponding dispersion panels are presented in Fig. 11 for the SB model scenario. The pressure–pressure component VSG and the associated dispersion panel for the SB model are displayed in Figs 12(a) and (b), respectively. The relative scale factor, representing the ratio of the maximum amplitudes relative to the vertical-to-vertical component VSG  $\mathcal{C}_{vv}$ , is noted at the bottom of each individual VSG in Fig. 10.

From Figs 10 and 11, the vertical-to-radial ( $C_{vr}$ ) and vertical-to-vertical ( $C_{vv}$ ) components exhibit dispersive modes of both fundamental and higher-order Scholte waves, as well as guided P-wave modes, with their lower frequencies travelling faster than higher frequencies. Due to their dispersive nature, the lower-frequency modes of these waves, characterized by longer wavelengths, penetrate deeper into the subsurface. Because the deeper layers have higher seismic velocities compared to the shallower layers, this causes the lower-frequency waves to propagate faster as they sample regions of higher velocity. Among the Scholte- and guided

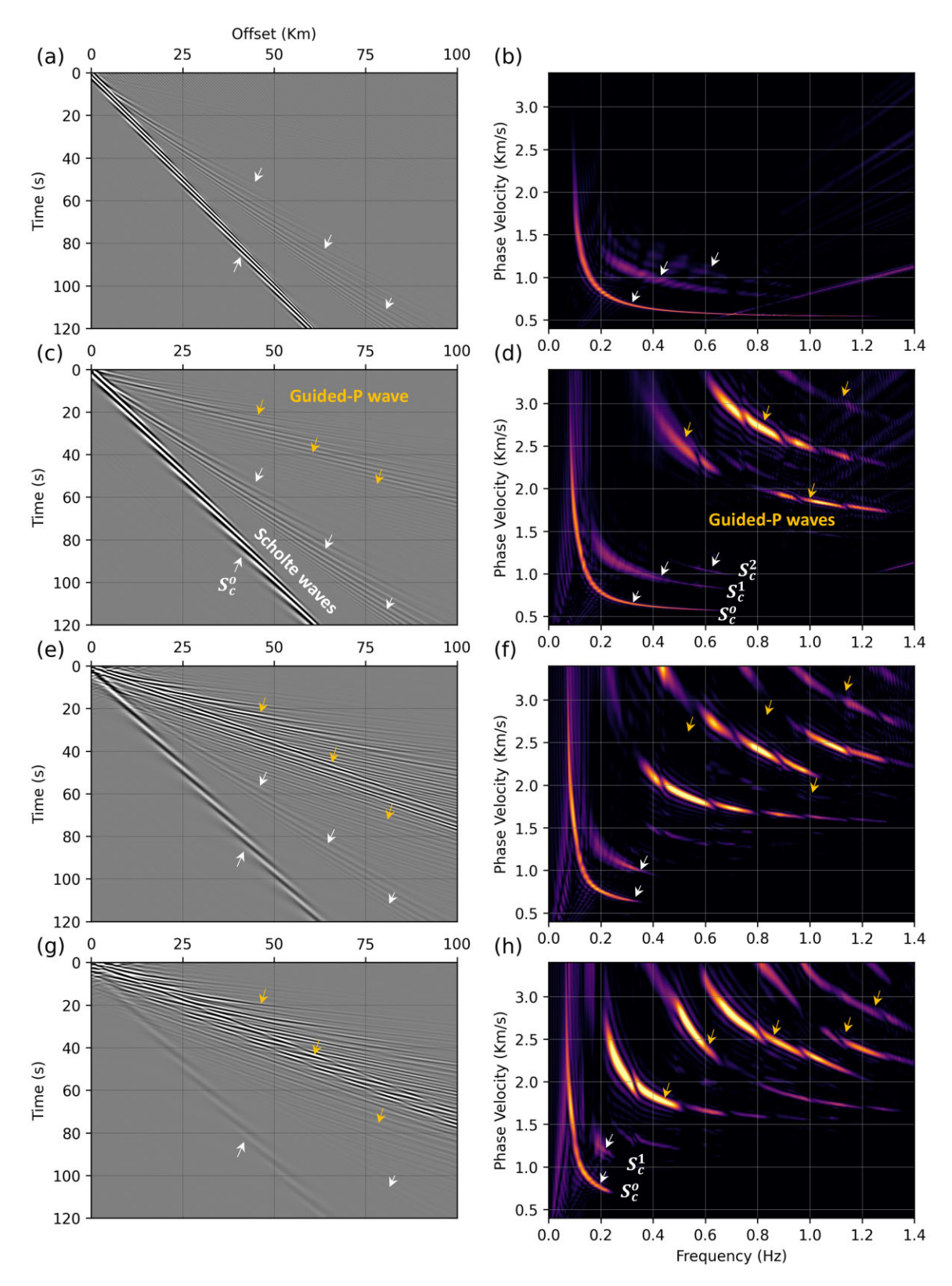


**Figure 7.** Vertical-component VSGs (left column) with corresponding dispersion panels (right column) for the SB model (see Table 2) with water depths of: (a, b) 0.25 km, (c, d) 0.75 km, (e, f) 1.50 km and (g, h) 2.25 km. Scholte and guided *P*-wave modes are highlighted by white and yellow arrows, respectively.

P-wave modes in  $\mathcal{C}_{vv}$  and  $\mathcal{C}_{vv}$  VSG, the fundamental-mode Scholte wave is the most dominant. At least two overtones of Scholte waves are also visible, although they appear to be weaker than the fundamental mode as indicated by their corresponding dispersion panels (Figs 11d and f).

The radial-to-radial ( $\mathcal{C}_{rr}$ ) VSG, shown in Fig. 10(a), exhibits intriguing behaviour. In particular, the higher-order Scholte wave modes are more pronounced than the fundamental mode ( $S_c^0$ ), with at least three overtones ( $S_c^1$ ,  $S_c^2$ ,  $S_c^3$ ) clearly visible in the corresponding dispersion panel (Fig. 11a). Observations of Scholte

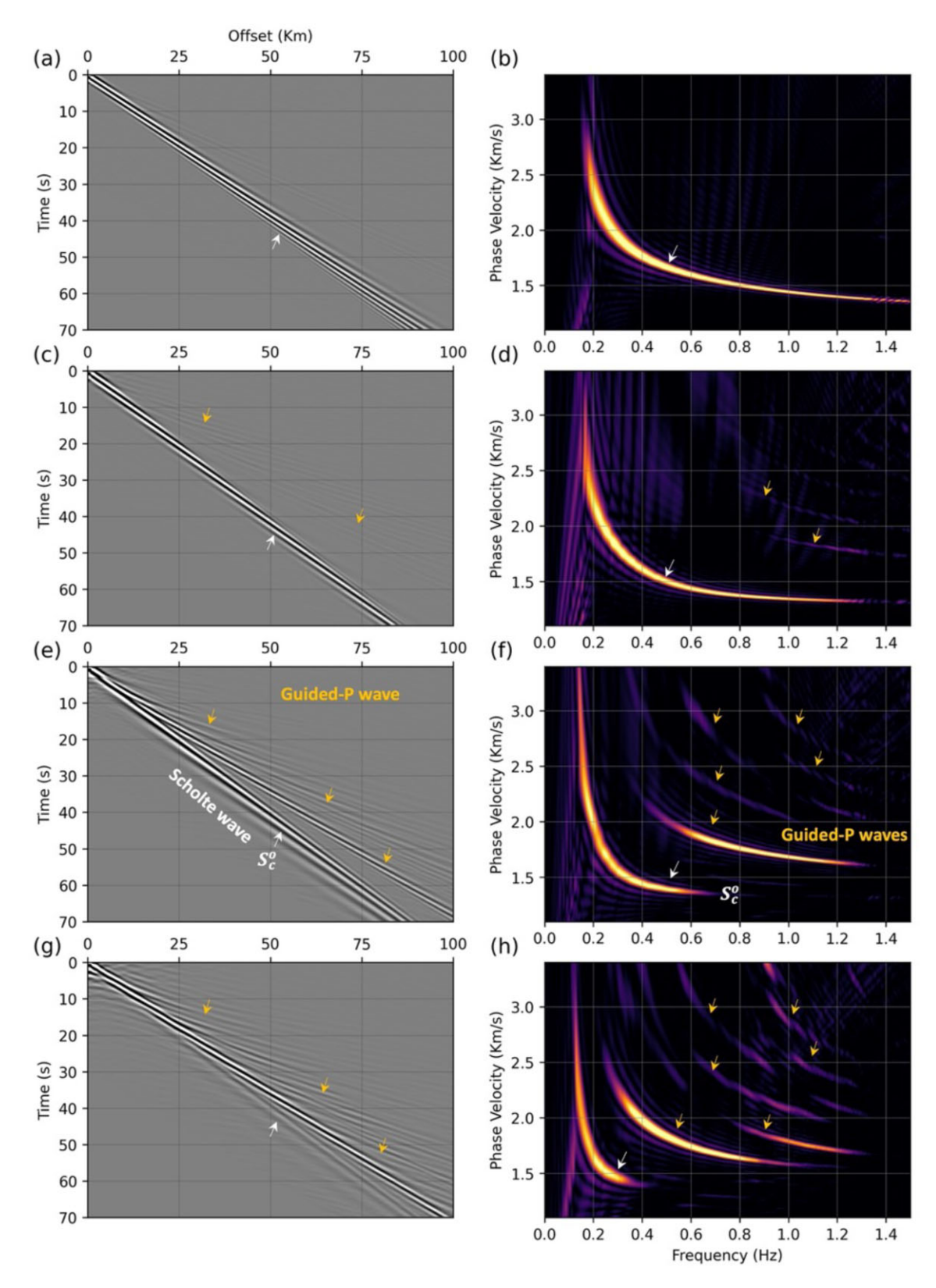


**Figure 8.** Vertical-component VSGs (left column) with corresponding dispersion panels (right column) for the HB model (see Table 2) with water depths of: (a, b) 0.25 km, (c, d) 0.75 km, (e, f) 1.50 km and (g, h) 2.25 km. Scholte and guided *P*-wave modes are highlighted by white and yellow arrows, respectively.

waves from four-component OBS recordings using a towed airgun source (e.g. Ritzwoller & Levshin 2002; Du *et al.* 2020; Wang *et al.* 2020, 2022; Shi *et al.* 2023) have commonly revealed an uneven distribution of dispersive energy across the four components of the

Scholte wavefield. The radial-component recording contains more energy from higher-order Scholte wave modes, while the vertical component is dominated by dispersive energy from the fundamental mode. This suggests that the fundamental mode is approximately

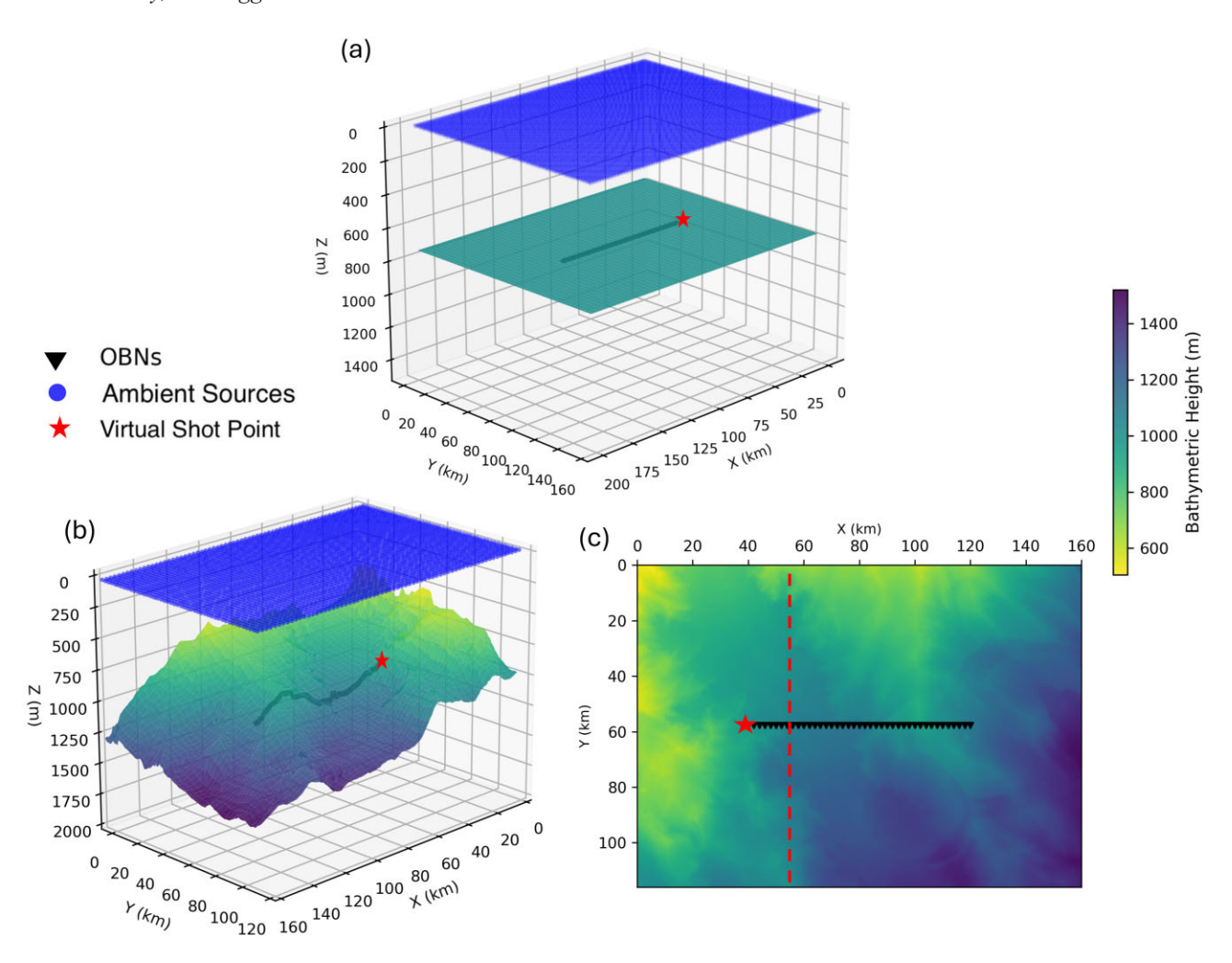


Figure 9. Secondary microseism sources, OBNs and virtual shot point location for (a) flat bathymetry, (b) variable bathymetric profile and (c) plane view of the variable bathymetry shown in panel (b). Dotted line in panel (c) corresponds to the velocity model cross-section shown in Fig. 16. The secondary microseism sources (blue dots) are uniformly distributed as pressure sources over the sea surface.

vertically polarized, whereas the higher modes tend to exhibit horizontal polarization. Consequently, as observed here, the  $\mathcal{C}_{vv}$  component contains more fundamental-mode contributions, while the  $\mathcal{C}_{rr}$  component contains more higher-mode contributions.

Because the source distribution is perfectly symmetric in the transverse direction relative to the receiver line (see Fig. 9a), the guided P- and Scholte-wave energy cancels out entirely in the transverse component recordings due to summation over this isotropic source distribution. Additionally, no Love waves are observed in any of the simulated transverse component VSGs shown in Fig. 10, as they are not excited in a perfectly horizontal, layered and isotropic medium with an isotropic secondary microseism source distribution (Gualtieri et al. 2020), as is the case here. As a result, the VSGs and dispersion panels presented in Figs 10 and 11 involving transverse component recordings-transverse-toradial ( $C_{tr}$ ), transverse-to-transverse ( $C_{tt}$ ) and vertical-to-transverse  $(C_{vt})$ —exhibit negligible energy, with no clear transversely polarized arrivals. Notable behaviour is also observed in the pressure-topressure  $C_{pp}$  VSG (Fig. 12a) for the SB model when compared with velocity VSGs in Fig. 10. The Scholte-wave energy is distributed unevenly between the velocity and pressure components. The velocity components exhibit stronger Scholte-wave energy than the pressure component. The fundamental and higher-order Scholte modes are

visibly absent in Figs 9(a) and (b), while the guided P waves appear strong. A weak  $S_c^0$  wave mode is discernible in the corresponding pressure dispersion panel in Fig. 12(b), though it is otherwise difficult to identify. A similar observation was reported by Wang et al. (2022) in the Yellow Sea, China, where active-source Scholtewave data recorded by multicomponent ocean-bottom seismometers on a soft ocean bottom using an airgun source showed stronger energy in the velocity than the pressure component. More recently, VSGs and dispersion panels presented by Girard et al. (2023) from the Mississippi Canyon area in the Gulf of Mexico demonstrated the same behaviour. As shown by the Scholte-wave eigenfunctions in Klein (2003) and Shi et al. (2023), this phenomenon may be attributed to the exponential decay of the fundamental Scholte-wave amplitude with increasing distance from the seafloor interface into the water column, with higher frequencies decaying more rapidly. Higher-order Scholte modes decay even faster than the fundamental mode as the distance from the interface increases within the water layer.

The black arrows in the  $\mathcal{C}_{rr}$  VSG in Fig. 10(a) highlight several cross-mode terms resulting from the correlation between different surface-wave modes and/or guided P modes, which would otherwise be absent if the conditions for Green's function retrieval through ambient seismic interferometry were satisfied (Pandey  $et\ al.\ 2025$ ).

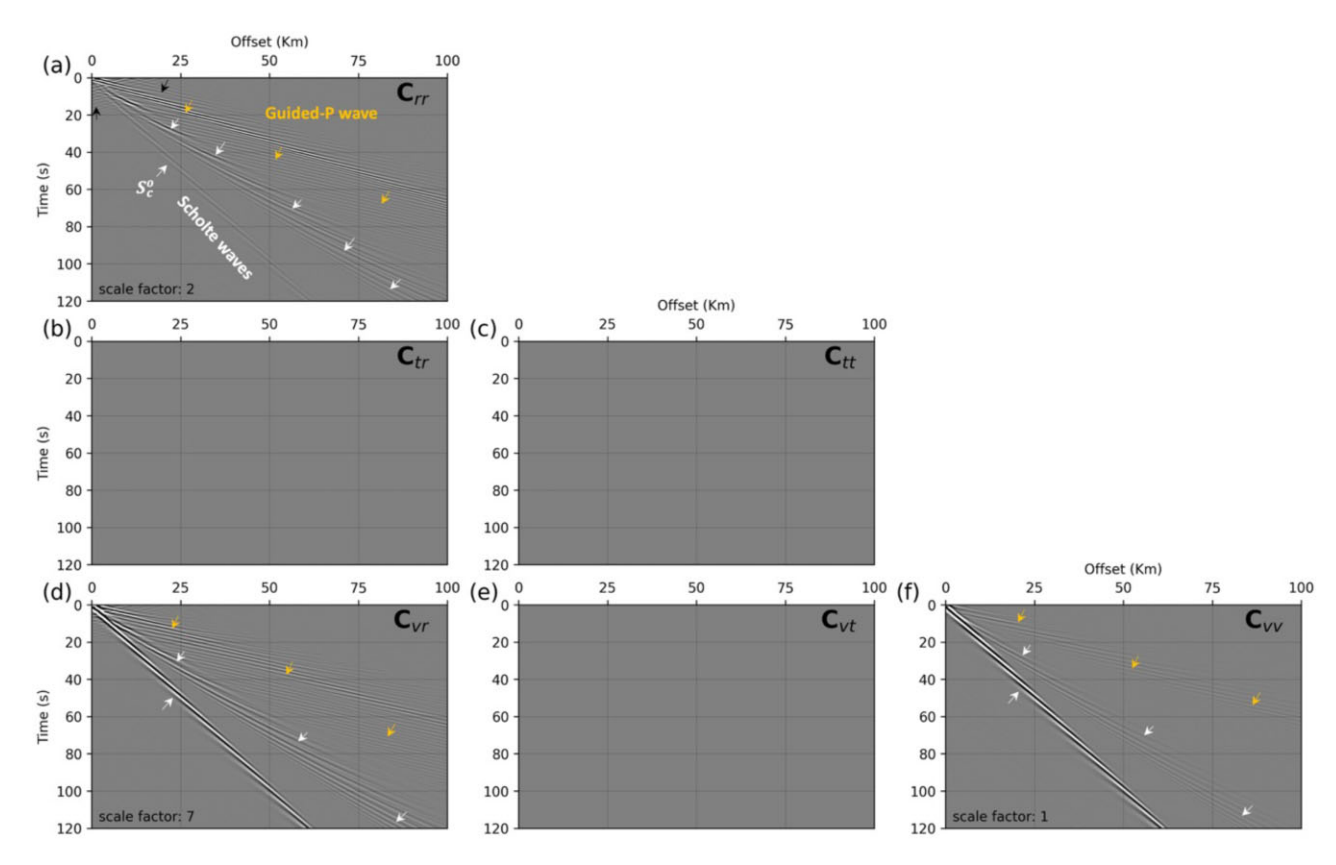


Figure 10. VSG Tensor components: (a)  $C_{rr}$ , (b)  $C_{tr}$ , (c)  $C_{tt}$ , (d)  $C_{vr}$ , (e)  $C_{vt}$  and (f)  $C_{vv}$  for the SB model (see Table 2) and a flat bathymetry with constant 0.75 km water depth. Scholte and guided P-wave modes are highlighted by white and yellow arrows, respectively. Black arrows represent cross-mode terms. The relative amplitudes between VSGs are not preserved; however, the scaling of each panel relative to  $C_{vv}$  is shown at the bottom of each panel.

These cross-mode terms are less prominent in the  $\mathcal{C}_{vr}$  VSG and are least evident in the  $\mathcal{C}_{vv}$  VSG (Fig. 10). This is because the guided P and Scholte waves in radial–radial component VSGs have lower energy due to their partial cancellation in radial direction, caused by the isotropic source distribution. As a result, the cross-mode terms in the horizontal components are present with energy levels comparable to the fundamental and higher-order Scholte and guided P modes. Conversely, in the vertical–vertical component VSG, wave-mode energy combines constructively, significantly weakening the cross-mode terms compared to the fundamental and higher-order Scholte and guided P modes.

Fig. 13 shows the velocity VSG tensor components, while Fig. 14 presents the corresponding dispersion panels for the HB model scenario. Figs 15(a) and (b), respectively, display the pressurecomponent VSG and the associated dispersion panel for the HB model. The HB model case velocity VSGs in Fig. 13 and corresponding dispersion panels in Fig. 14 show similar behaviour to that observed in the SB model case, except for the lack of higherorder Scholte wave modes that were present in the SB case. The  $\mathcal{C}_{pp}$  VSG (Fig. 15a) also shows the presence of Scholte waves, as opposed to their notable absence in  $C_{pp}$  VSG in the SB case (Fig. 12a). This feature is consistent with observations from the Gulf of Mexico Amendment OBN array, where the ocean bottomas sensed by low-frequency ambient wavefield—appears hard, and Scholte waves are clearly discernible in both the  $\mathcal{C}_{pp}$  VSG and the associated dispersion panel (Girard et al. 2024). Scholte-wave velocities in the HB model are significantly faster ( $\approx 1.45 \text{ km s}^{-1}$ at 0.6 Hz, as seen in the  $C_{vv}$  dispersion panel in Fig. 14f), compared to the SB case ( $\approx$ 0.6 km s<sup>-1</sup> at 0.6 Hz, as seen in the  $\mathcal{C}_{vv}$ 

dispersion panel in Fig. 11f), due to the higher  $v_s$  at and below the ocean bottom (see Table 2). The  $\mathcal{C}_{vr}$ ,  $\mathcal{C}_{vv}$  and  $\mathcal{C}_{rr}$  components show dispersive fundamental Scholte and guided P-wave modes. No Scholte-wave overtones are present, as evident in the dispersion panels presented in Fig. 14. Guided P-wave modes are most pronounced in the  $\mathcal{C}_{rr}$  VSG, with black arrows highlighting the cross-mode events.

### 3.3.2 3-D model with variable bathymetry and smoothly varying vertical and horizontal velocities

We next assess the impact of variable bathymetry and 3-D velocity structure on ocean-bottom cross-correlations, with a particular focus on generating and recording of Love waves due to secondary microseism sources acting on the ocean surface. The mesh configuration for this synthetic model was adapted to follow the bathymetric profile shown in Fig. 9(b). The velocity models, using parameters listed in Table 2, were initially generated with flat bathymetry and regular grid spacing. It was subsequently adjusted to conform to the bathymetric profile, introducing smoothly varying horizontal velocities, as shown in Fig. 16.

Primary microseisms, resulting from the direct interaction of ocean waves with the seafloor at longer periods, can generate Love waves through coupling with the seafloor (Fukao *et al.* 2010; Saito 2010). However, secondary microseisms, characterized by pressure-like sources acting at the ocean surface, cannot directly explain the presence of Love waves in cross-correlations of horizontal-component ocean-bottom recordings. Two main hypotheses have been proposed to account for the generation of Love

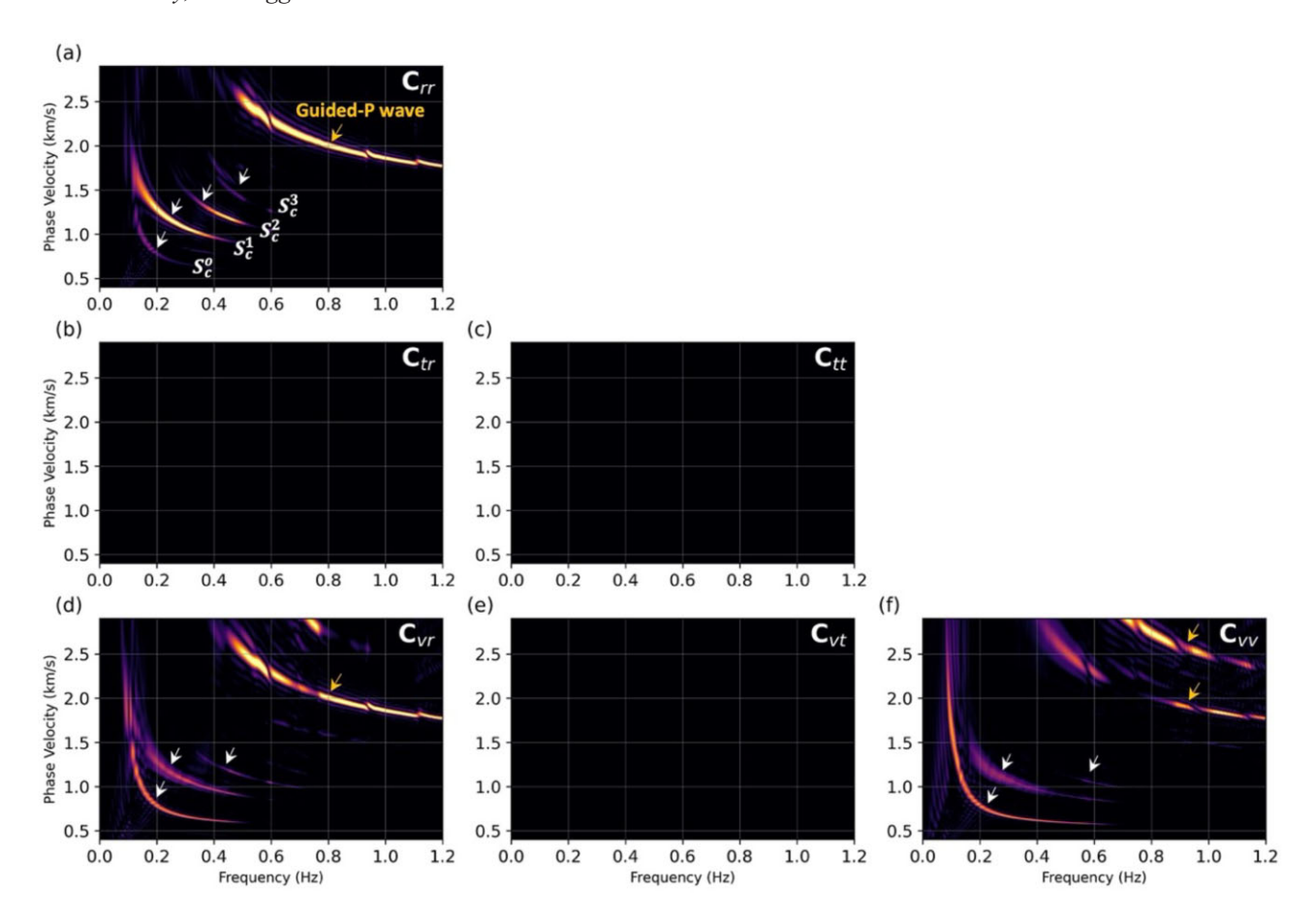


Figure 11. Dispersion panels for VSGs in Fig. 10. (a)  $C_{rr}$ , (b)  $C_{tr}$ , (c)  $C_{tt}$ , (d)  $C_{vr}$ , (e)  $C_{vt}$  and (f)  $C_{vv}$  components. Scholte and guided P-wave modes are highlighted by white and yellow arrows, respectively.

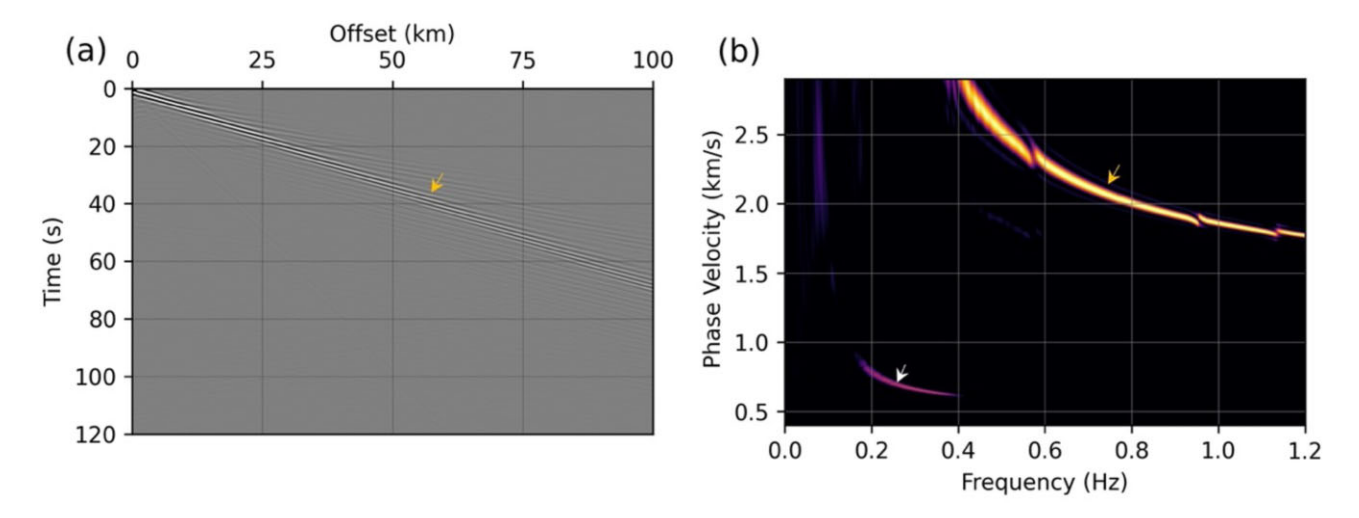


Figure 12. Pressure-to-pressure  $C_{pp}$  (a) VSG and (b) dispersion panel for SB model parameters in Table 2 with constant 0.75 km bathymetry. Scholte and guided P-wave modes are highlighted by white and yellow arrows, respectively.

waves from secondary microseism sources. The first hypothesis suggests that bathymetric variations in the source regions play a key role. Such variations can partition the vertical second-order pressure force into two components: one perpendicular to the local

bathymetric slope, and being responsible for Scholte waves, the other tangent to the slope and being responsible for Love waves. The second hypothesis attributes the generation of Love waves to lateral heterogeneity within the Earth, which can cause scattering and

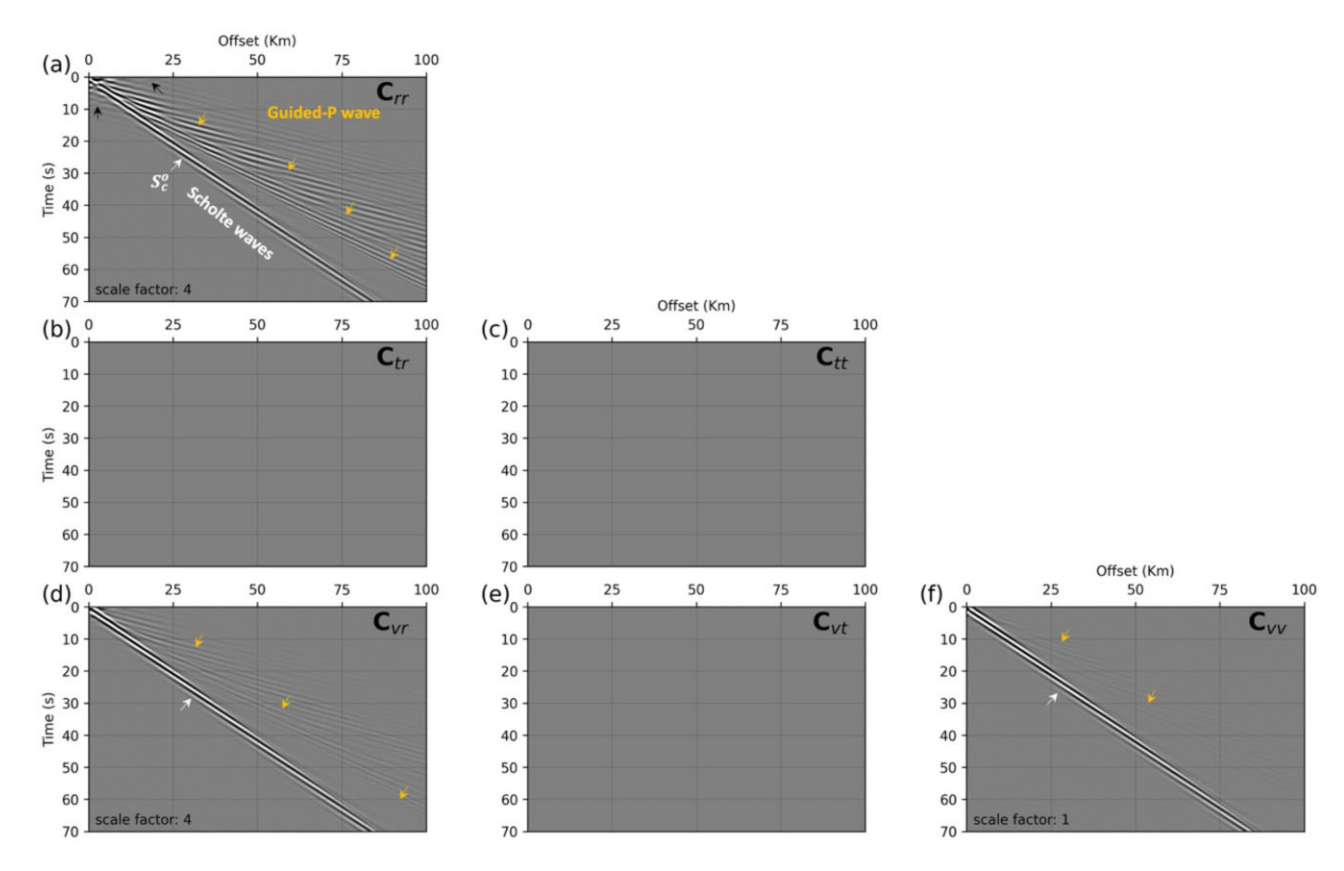


Figure 13. VSG Tensor components: (a)  $C_{TT}$ , (b)  $C_{LT}$ , (c)  $C_{tt}$ , (d)  $C_{VT}$ , (e)  $C_{vt}$  and (f)  $C_{vv}$  for the HB model parameters in Table 2 and a flat bathymetry with constant water depth of 0.75 km. Scholte and guided P-wave modes are highlighted by white and yellow arrows, respectively. Black arrows represent cross-mode terms. The relative amplitudes between VSGs are not preserved; however, the scaling of each panel relative to  $C_{vv}$  is shown at the bottom of each panel.

focusing/defocusing effects (Iyer 1958; Haubrich & McCamy 1969; Gualtieri et al. 2020; Le Pape et al. 2021). Additionally, Rayleighto-Love wave conversion at ocean—continent boundaries may also contribute, though only a small percentage of incident Rayleighwave energy is converted into Love-wave energy (Gregersen & Alsop 1976). In contrast, in the absence of bathymetric variations and at low frequencies relative to ocean depth, each pressure source behaves like a vertical point force acting on a flat surface (Gualtieri et al. 2013). For a 1-D Earth model with only vertical velocity variations and flat bathymetry, as considered in the previous section, a vertical force will not generate shear motion and thus Love waves were not observed in any VSG simulation.

To incorporate these considerations, we employ velocity models that vary smoothly in both horizontal and vertical directions (Fig. 16) and include a high-resolution bathymetry profile from the northern Gulf of Mexico. The bathymetric profile, displayed in 3-D in Fig. 9(b) and in 2-D in Fig. 9(c), spans an area of 160 km  $\times$  120 km ( $x \times y$ ). The profile has a shallowest depth of approximately 0.5 km in the northeastern corner and a deepest depth of approximately 1.5 km in the southwestern corner of the grid. This detailed bathymetric grid was generated from 3-D seismic surveys conducted in the Northern Gulf of Mexico deep water region and is publicly available from Bureau of Ocean Energy Management (BOEM) (2014). We again consider the SB and HB scenarios with the velocities and densities at the ocean bottom for the two models given in Table 2.

As in previous sections, the receivers for velocity and pressure cross-correlation simulations are positioned 10 m below and 10 m above the bathymetric surface, respectively. These receivers are

aligned along a single line parallel to the *x*-axis and span an 80 km offset. The pressure-type sources are distributed isotropically across the ocean surface (see Figs 9a and b). Table 3 presents this synthetic model settings. The virtual shot point is located at the nearest end of the receiver array, as indicated by the stars in Figs 9(a) and (b).

Fig. 17 illustrates the velocity VSG tensor components, while Fig. 18 shows the corresponding dispersion panels for the SB scenario. The first three theoretical Scholte mode dispersion curves, calculated using the 1-D velocity model at the virtual shot location, are also shown in Fig. 18(g) as dashed curves. Because the velocity CCF tensor is now asymmetric due to bathymetric variations, even though the source distribution is isotropic, we present all of the  $3 \times 3$  VSG tensor components and the associated dispersion panels. In all VSG components shown in Fig. 17, we observe dispersive fundamental and higher-order Scholte and guided P-wave modes, although with varying energy, similar to the flat bathymetry scenario. Scholte wave modes are indicated by white arrows, while guided P modes are marked by yellow arrows in Fig. 17(a). VSGs that include transverse recording as one of their components— $C_{rt}$ ,  $C_{tr}$ ,  $C_{tt}$ ,  $C_{tv}$ ,  $C_{vt}$ —exhibit significantly lower energy with relative scale factors exceeding 100, (see Fig. 17) compared to VSGs with radial and vertical components— $C_{rr}$ ,  $C_{rv}$ ,  $C_{vr}$  and  $C_{vv}$ . This is again due to the summation over the source distribution, which is perfectly symmetric in the transverse direction relative to the receiver line (Fig. 9b). However, in the presence of variable bathymetry, this symmetry does not result in the perfect cancellation of wave-mode energy in the transverse component recordings, resulting in the presence of residual energy. Consequently, VSGs that include transverse component recordings exhibit lower energy compared to those with

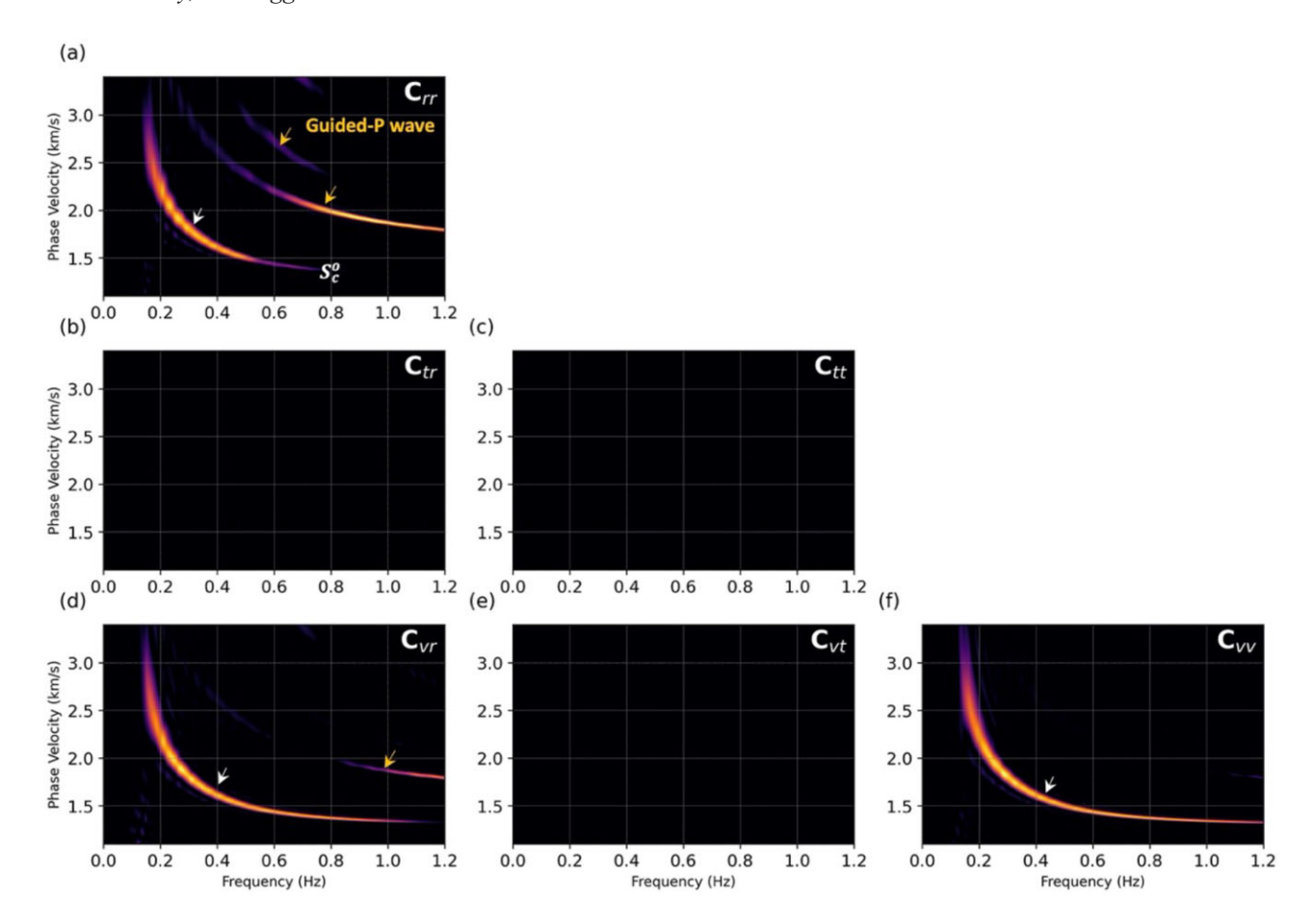


Figure 14. Dispersion panels for VSGs in Fig. 13. (a)  $C_{rr}$ , (b)  $C_{tr}$ , (c)  $C_{tt}$ , (d)  $C_{vr}$ , (e)  $C_{vt}$  and (f)  $C_{tt}$  components. Scholte and guided P-wave modes are highlighted by white and yellow arrows, respectively.

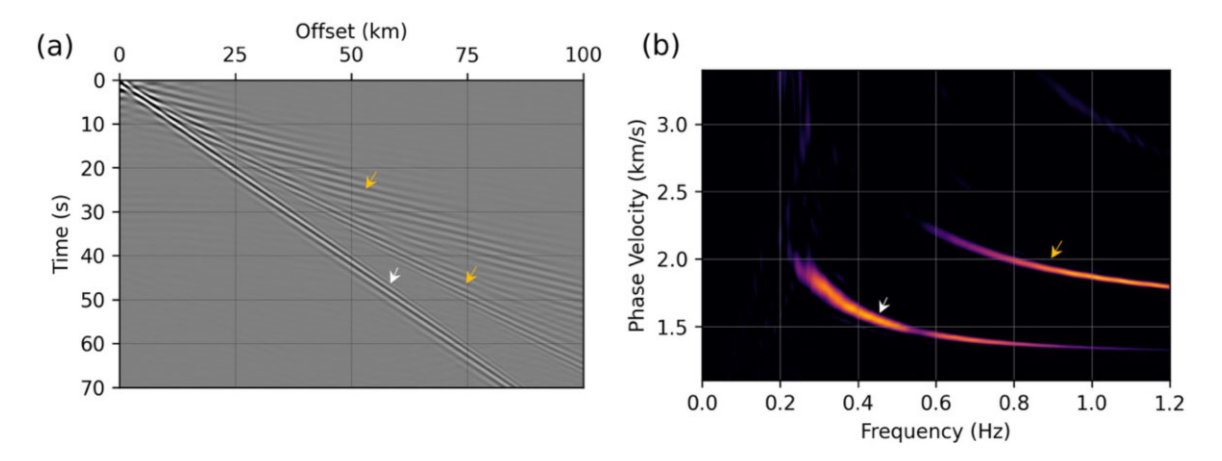


Figure 15. Pressure-to-pressure component  $C_{pp}$  (a) VSG and (b) dispersion panel for HB model parameters in Table 2 and a flat bathymetry with constant water depth of 0.75 km. Scholte and guided P-wave modes are highlighted by white and yellow arrows, respectively.

radial and vertical components. As a result, residual Scholte wave and guided P energy appears in the transverse component VSGs as well, as indicated by the white and yellow arrows, respectively, in Figs 17(b), (e) and (h) and their corresponding dispersion panels in Figs 18(b), (e) and (h).

Higher-order Scholte modes are again more prominently observed in the  $\mathcal{C}_{rr}$  and  $\mathcal{C}_{tt}$  components compared to the fundamental

Scholte mode, as evident from the associated dispersion panels in Fig. 18. The dispersion panels in Fig. 18 also highlight the more complex nature of guided *P* modes in the variable bathymetry case compared to the flat bathymetry scenario dispersion panels shown in Fig. 11.

As expected, we observe Love waves in VSGs with transverse component recording as other receivers— $C_{rt}$ ,  $C_{tt}$  and  $C_{vt}$ . These Love

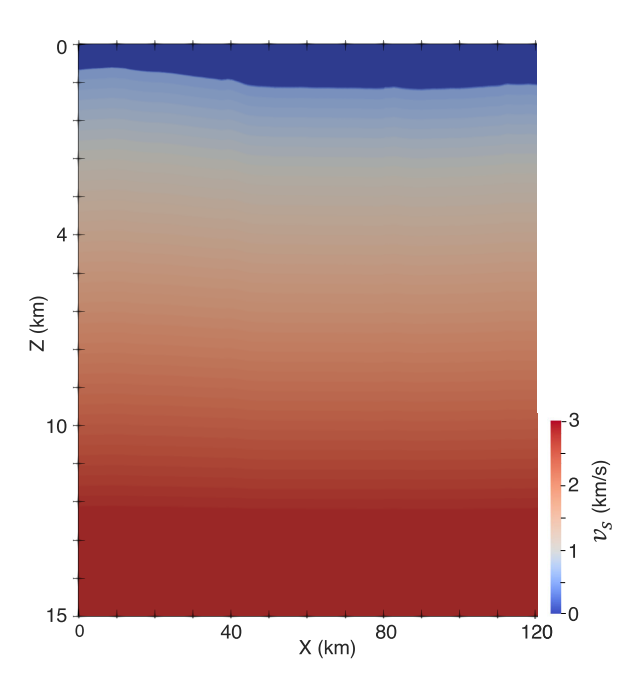


**Figure 16.** Cross-section of the  $v_s$  model down to 15 km depth, extracted along the dotted line in Fig. 9(c) and used for modelling in Section 3.3.2. Axes are not to scale; the vertical axis is exaggerated by a factor of 10 to highlight the subtle horizontal velocity variations, which broadly follow the seafloor bathymetry down to approximately 10 km depth.

waves are marked in Figs 17(b) ( $C_{rt}$  VSG), 17(e) ( $C_{tt}$  VSG) and 17 (h) ( $C_{vt}$  VSG) with their most prominent appearance in the  $C_{vt}$  component. The Love waves travel at slightly higher velocities than the fundamental Scholte waves, as evident from comparing arrival times at the far end of the time axis of the VSG panels of Fig. 17(h) (containing Love waves) and Fig. 17(i) (containing fundamentalmode Scholte waves). This distinction is more apparent in the zoomed-in section of the bottom-row dispersion panels between phase velocities of 0.5–0.8 km s<sup>-1</sup> in Fig. 18, as shown in Fig. 19, which highlights a faster Love wave mode with a phase velocity of 0.70 km s<sup>-1</sup> at 0.4 Hz, compared to the fundamental Scholte wave mode with a phase velocity of 0.62 km s<sup>-1</sup> at the same frequency. This is further confirmed by the theoretical Love wave dispersion curve, shown as dotted curves and calculated using the 1-D velocity model at the virtual shot location, overlain on the dispersion panel in Fig. 18(h). Real ambient seismic cross-correlation examples above 0.1 Hz over a hydrocarbon reservoir in the Norwegian North Sea, as presented in Bussat & Kugler (2011), also show the presence of Love waves in the  $\mathcal{C}_{tt}$  VSG component; however, no cross-component VSGs are presented therein. Similarly, de Ridder & Biondi (2013a) reported the presence of Love waves in the  $C_{tt}$ VSG between 0.18 and 1.75 Hz over the Valhall oil field offshore Norway. They further observed that the transverse-vertical and transverse-radial VSGs are significantly weaker than the others—an observation consistent with the cross-component VSGs discussed

Because we have oriented ambient sources in the transverse (+y) direction to the receiver line (see Fig. 9), they should ideally excite Love waves in the radial direction. In theory, these Love waves would cancel out due to a symmetric source in the opposite transverse (-y) direction. However, due to variable bathymetry, and because our transverse and radial components are aligned with the horizontal plane rather than the local bathymetric slope—and the

vertical (v) direction is not perpendicular to the slope—we expect some residual Love wave energy to leak into the radial and vertical components. These residual Love waves are indicated by green arrows in the  $\mathcal{C}_{rv}$  and  $\mathcal{C}_{vv}$  VSGs in Figs 17(c) and (e), respectively. We do not detect them in other VSGs involving radial and vertical component recordings (e.g.  $\mathcal{C}_{rr}$  in Fig. 17a and  $\mathcal{C}_{vr}$  in Fig. 17g) likely because their amplitudes are too weak. The black arrow in Fig. 17(h) marks a strong cross-mode term, identified by its non-zero crossing. Red arrows in Figs 17(c) and (i) indicate numerical noise caused by Scholte-wave boundary reflections due to imperfect PMLs.

The pressure–pressure VSG and associated dispersion panel are displayed in Figs 20(a) and (b), respectively. The pressure VSG,  $\mathcal{C}_{pp}$ , is dominated by guided P waves. The fundamental and higher-order overtones Scholte waves are notably absent. Although very weak fundamental Scholte mode energy is present in the  $\mathcal{C}_{pp}$  dispersion panel in Fig. 12(b), it is otherwise difficult to identify in the associated VSG.

Fig. 21 shows the velocity VSG tensor components for the HB scenario, while their corresponding dispersion panels are presented in Fig. 22. The theoretical fundamental Scholte mode dispersion curve, calculated using the 1-D velocity model at the virtual shot location, is also shown in Fig. 22(g) as dashed curve. The pressure VSG and the associated dispersion panel are displayed in Figs 23(a) and (b), respectively. Similar to the observations described above for the SB case, Fig. 21 reveals dispersive Scholte and guided P-wave modes, marked in Fig. 21(a), but no overtones of Scholte waves are present. These modes are more coherent in VSGs involving radial and vertical components— $\mathcal{C}_{rr},~\mathcal{C}_{rv},~\mathcal{C}_{vr}$  and  $\mathcal{C}_{vv}$ —as indicated by the corresponding dispersion panels in Fig. 22. In contrast, the energy in VSGs involving transverse components— $C_{rt}$ ,  $C_{tr}$ ,  $C_{tt}$ ,  $C_{tv}$ and  $C_{vt}$ —is significantly lower (see scale factors in Fig. 21). Love waves are identified in the  $C_{rt}$ ,  $C_{tt}$  and  $C_{vt}$  VSGs and in the corresponding dispersion panels, with their most prominent presence in the  $\mathcal{C}_{vt}$  component, consistent with the SB case. The presence of Love waves is further confirmed by the theoretical Love wave dispersion curve overlain as a dotted curve on the dispersion panel in

In contrast to the SB scenario,  $C_{pp}$  for HB case (Fig. 23a) exhibits clearly identifiable fundamental-mode Scholte-wave energy. Guided P modes also are present and clearly visible in the  $C_{pp}$  dispersion panel presented in Fig. 23(b). The pressure and vertical-velocity VSGs and their dispersion panels from this HB scenario bear a strong resemblance to those observed from the Gulf of Mexico Amendment OBN array ambient seismic data (Girard et al. 2024). In that study, the ocean bottom, interpreted using low-frequency (sub-1 Hz)  $S_c^0$  waves, is hard with average near-seafloor shear velocities exceeding 1.5 km s<sup>-1</sup>.

The black arrows in the  $\mathcal{C}_{rr}$  VSG in Fig. 17(a) and the  $\mathcal{C}_{tr}$  VSG in Fig. 21(d) highlight several spurious cross-mode terms. These are present in nearly all VSGs in Figs 17 and 21, albeit with varying amplitudes and being more pronounced in some cases than in others.

#### 3.4 Inhomogeneous ambient source distribution

The distribution of ambient source energy, as determined through data back projection or beamforming in recent surface-wave studies, reveals that ambient energy is typically neither isotropic nor stationary. Instead, ambient source energy distributions often exhibit significant azimuthal and temporal variations (Stehly *et al.*)

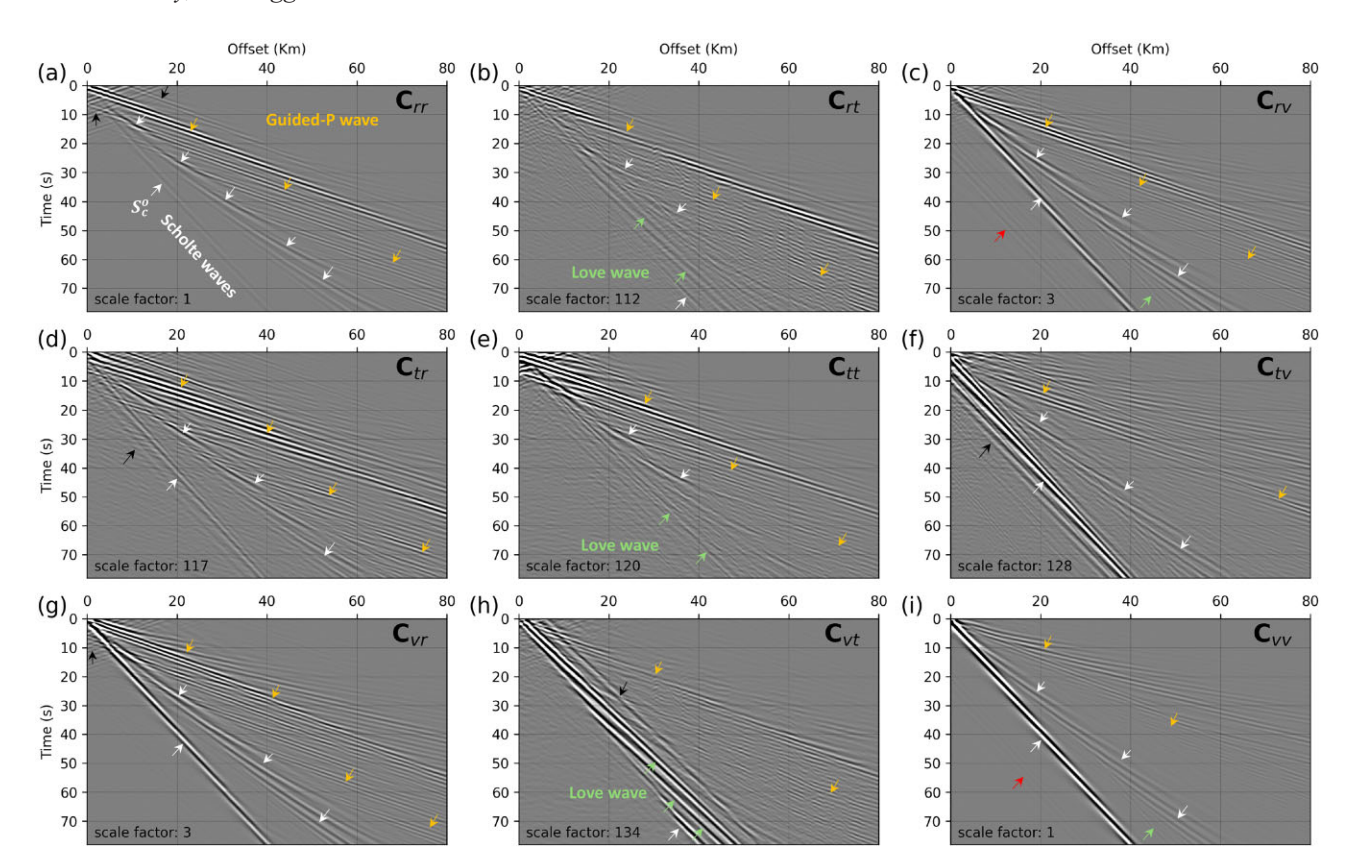


Figure 17. VSG tensor components: (a)  $\mathcal{C}_{rr}$ , (b)  $\mathcal{C}_{rt}$ , (c)  $\mathcal{C}_{rv}$ , (d)  $\mathcal{C}_{tr}$ , (e)  $\mathcal{C}_{tt}$ , (f)  $\mathcal{C}_{vv}$ , (g)  $\mathcal{C}_{vv}$ , (h)  $\mathcal{C}_{vt}$  and (i)  $\mathcal{C}_{vv}$  for the 3-D velocity structure with soft ocean bottom and variable bathymetry. Scholte and guided P-wave modes are highlighted by white and yellow arrows, respectively, while Love waves are denoted by green arrows. Black arrows represent cross-mode terms. Red arrows indicate numerical noise caused by Scholte-wave boundary reflections due to imperfect PMLs. The relative amplitudes between VSGs are not preserved; however, the scaling of each panel relative to  $\mathcal{C}_{vv}$  is shown at the bottom of each panel.

2006; Yang & Ritzwoller 2008; Yao *et al.* 2009). These azimuthal source strength variations can markedly affect not only the energy of different wave modes but also their excitation, particularly for Love waves.

To illustrate this, we consider an example of an inhomogeneous secondary-microseism source distribution, with the maximum source strength oriented at a northwesterly azimuth of  $135^\circ$ , as shown in Fig. 24(a). For this case, we focus on the  $\mathcal{C}_{vt}$  component VSG, as Love waves are observed most prominently on this component, as demonstrated in the previous section. We use a 3-D model with a soft bottom, variable bathymetry and OBNs positioned 10 m below the seafloor.

Figs 24(b)–(d) present the  $C_{vt}$  VSGs with relative amplitude scaling for OBN lines A, B and C, respectively, as indicated in Fig. 24(a). OBN line A is oriented along the direction of maximum source strength, line B is at a 45° angle and line C is orthogonal to the maximum source strength direction. When sources are aligned with the receiver line, as with line A, the Love waves are strongest, as shown in Fig. 24(b). For the receiver lines at 45° (line B) and orthogonal (line C), the Love waves are more weakly observed, as seen in Figs 24(c) and (d), than when compared to line A data in Fig. 24(b). This occurs because, for line A, the strong sources lie within the stationary phase region (Snieder 2004) and contribute to constructive interference. In contrast, for lines B and C, the sources contribute less effectively to the stationary phase integral. Residual fundamental Scholte mode is indicated by white arrow in Fig. 24(b). The black arrows in Figs 24(b)–(d) represent cross-modal terms. Note that these spurious arrivals are stronger in line C compared to line A due to their incomplete destructive interference, resulting from strong sources in the non-stationary phase region and their uneven distribution relative to the receiver line (Snieder *et al.* 2006; Halliday & Curtis 2008).

The presence of strong Love waves along the receiver line aligned with the direction of strong secondary microseism sources in this example, is consistent with the observations presented in Gualtieri et al. (2020). One hypothesis regarding the generation of Love waves from secondary microseisms states that Love waves with significant magnitude are generated in source regions with significant pressure power spectral density, provided there are bathymetric variations in the source region. In this scenario, the observed wave direction will point towards the strongest concentration of sources. Although Love waves cannot be generated at the source itself, the conversion from Rayleigh to Love waves occurs at depth due to heterogeneous Earth structure within the same geographic region where the strongest sources are located. Therefore, when looking for the strongest Love waves in the ocean-bottom sensor cross-correlation data, it is judicious to focus on the vertical-to-traverse component VSGs  $C_{vt}$  in the direction of the strongest ambient sources derived through backprojection or beamforming for the low-frequency ocean-bottom sensor data.

#### 4 DISCUSSION

We now discuss the implications of the observations made during the analysis of the controlling factors for using ambient seismic wavefields in long-wavelength structural imaging and elastic model

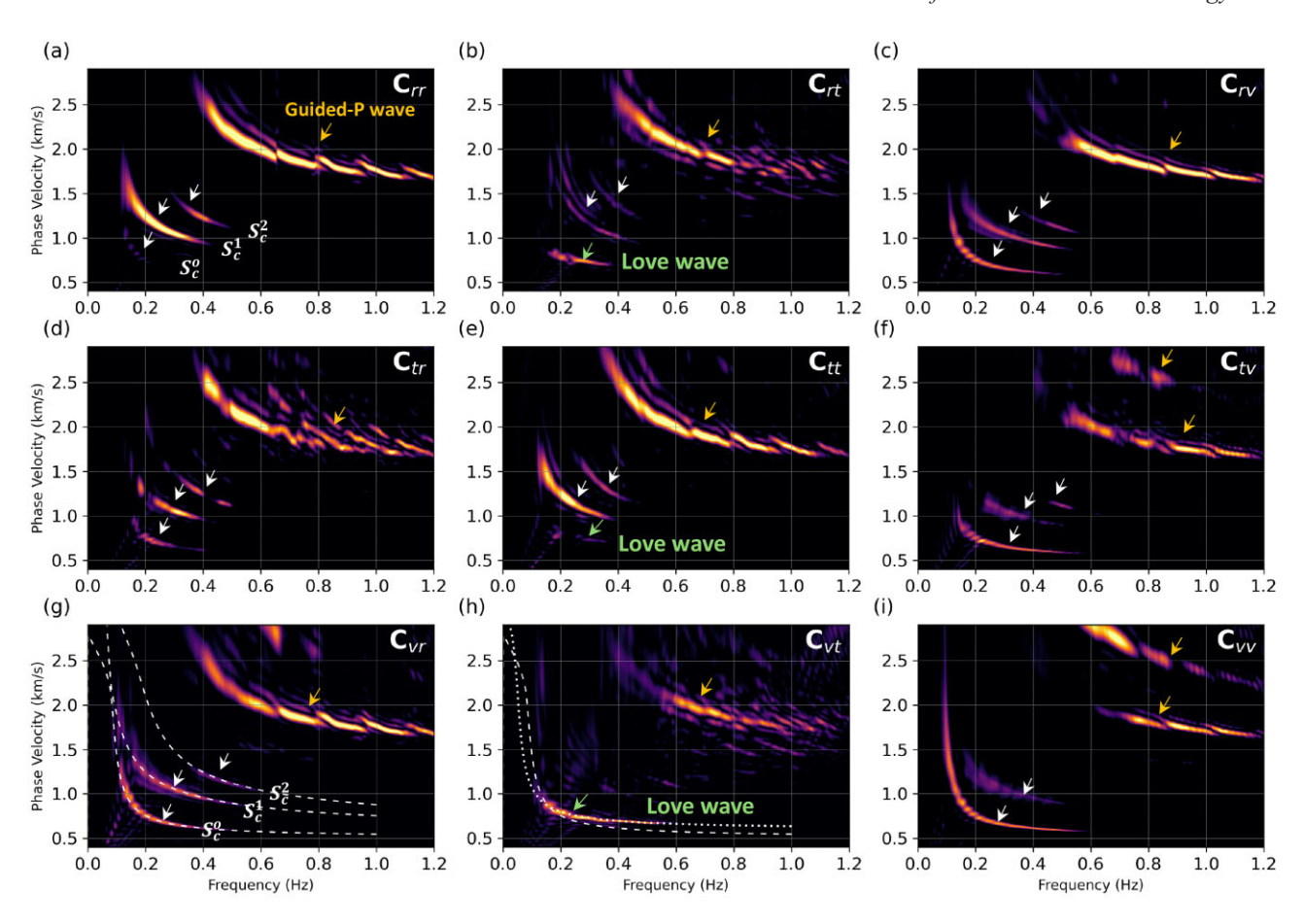


**Figure 18.** Dispersion panels for the VSGs shown in Fig. 17. (a)  $C_{rr}$ , (b)  $C_{rt}$ , (c)  $C_{rv}$ , (d)  $C_{tr}$ , (e)  $C_{tv}$ , (g)  $C_{vr}$ , (h)  $C_{vt}$  and (i)  $C_{vv}$  components. Scholte and guided *P*-wave modes are highlighted by white and yellow arrows, respectively, while Love waves are denoted by green arrows. The theoretical Scholte modes (dashed curves) are plotted in panels (g) and (h), and the Love wave mode (dotted curve) is plotted in panel (h).

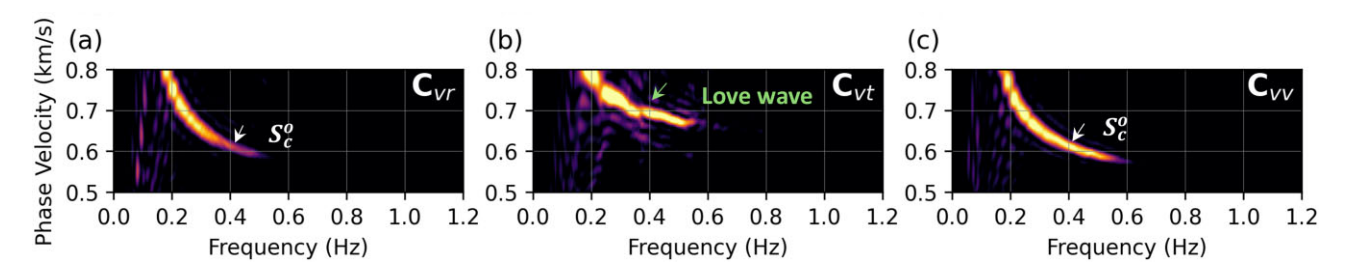


Figure 19. Zoomed-in section of the bottom-row dispersion panels between phase velocities of 0.5–0.8 km s<sup>-1</sup> in Fig. 18, highlighting a faster Love wave mode compared to the fundamental Scholte wave mode. (a)  $C_{vv}$ , (b)  $C_{vt}$  and (c)  $C_{vv}$ .

building. A key observation concerns the impact of guided *P*-wave modes on Scholte-wave frequency content due to truncation effects. The usable ambient frequency range typically recorded on ocean-bottom sensors spans from as high as 2.0 Hz to as low as 0.1 Hz (de Ridder & Biondi 2013a; Mordret *et al.* 2013; Girard *et al.* 2023, 2024). The dominant ambient energy between 0.1 and 1.0 Hz frequencies is generally generated by secondary microseism sources acting at the ocean surface. In shallow water where the ocean depth is much smaller than the wavelength corresponding to the source frequencies, guided *P* waves have a negligible effect on Scholte waves. This condition allows for broader frequency coverage and energy partitioning across the fundamental Scholte wave and higher-order modes whenever excited. In contrast, in deeper water where the wavelength is short compared to the ocean depth, *P*-wave propagation within the water layer significantly affects Scholte wave

mode generation and the associated frequency content. Guided P waves, generated by secondary microseism sources, undergo multiple reflections between the ocean surface and the sea floor. This phenomenon leads to their strong dispersion energy and the appearance of multiple modes in VSGs observations. Consequently, the Scholte-wave frequency range narrows due to high-frequency truncation in dispersion spectra and higher-order modes are visually suppressed.

This phenomenon is critical for surface-wave inversion using dispersion images. In surface-wave inversion, the modal structure and frequency bandwidth of extracted dispersion curves significantly influence both the accuracy and the maximum depth of the inversion. Incorporating higher-order modes into the inversion process can substantially enhance accuracy, improve model resolution, reduce non-uniqueness, facilitate convergence and enable deeper

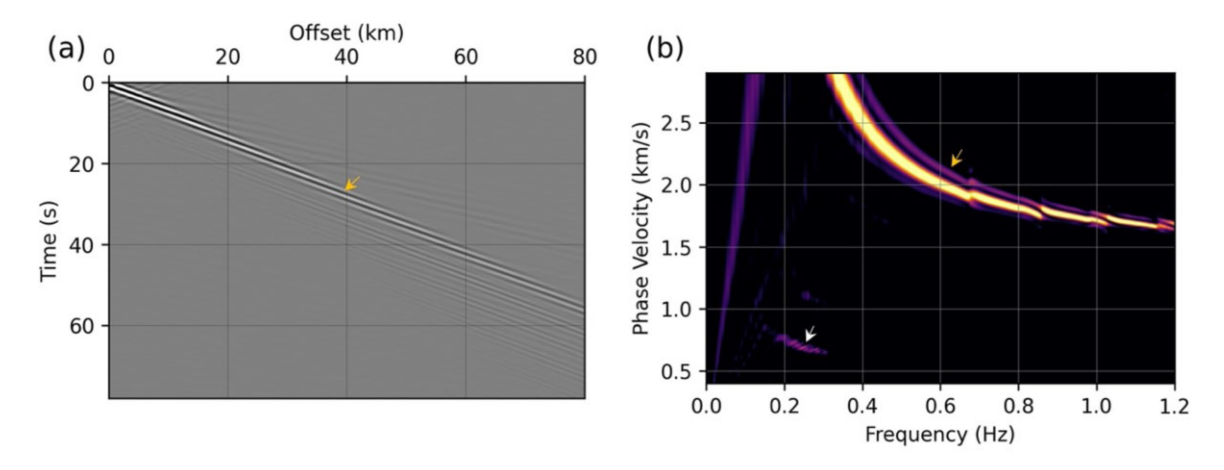


Figure 20. Pressure-to-pressure  $C_{pp}$  (a) VSG and (b) dispersion panel for the 3-D velocity structure for the SB model and variable bathymetry. Scholte and guided P-wave modes are highlighted by white and yellow arrows, respectively.

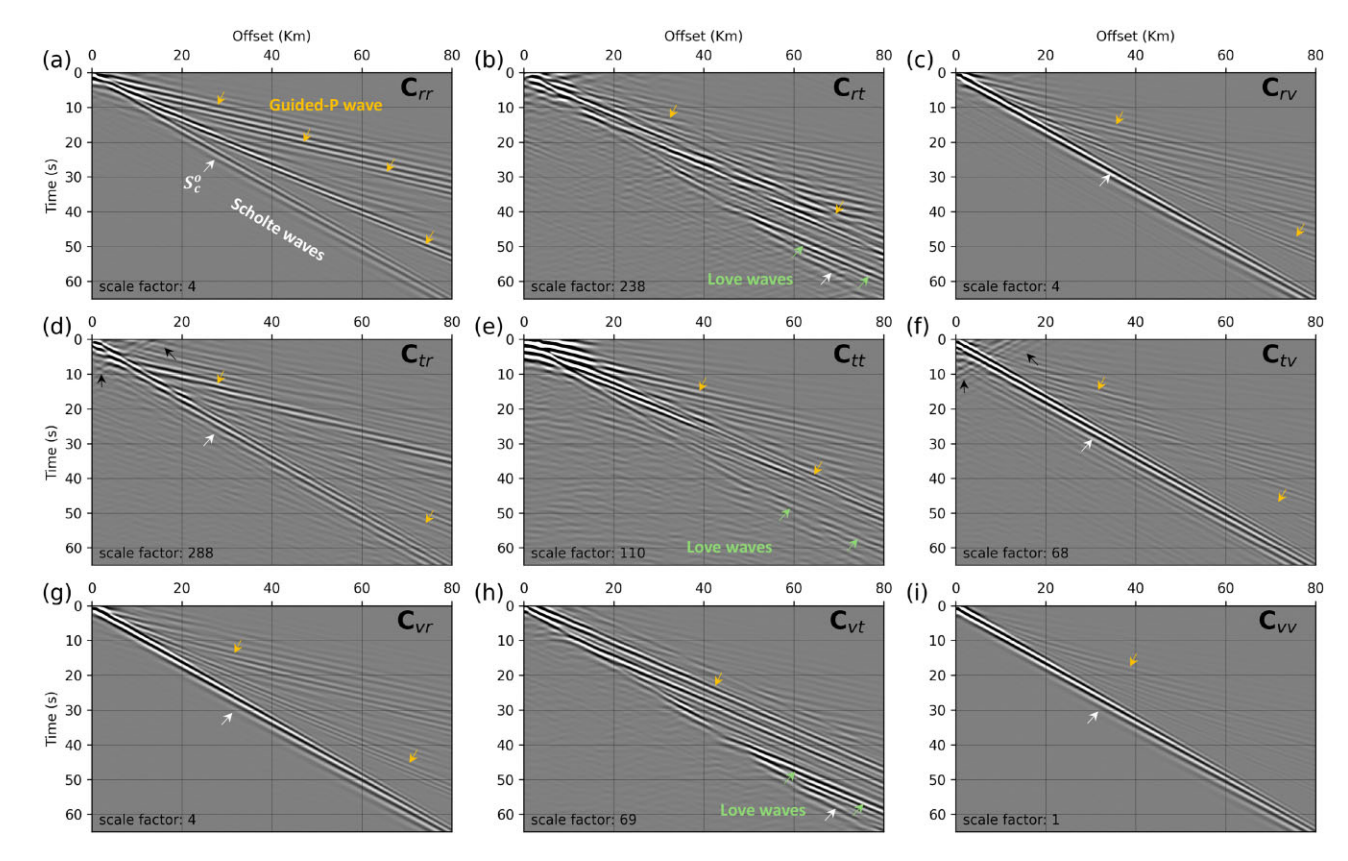


Figure 21. VSG Tensor components: (a)  $C_{rr}$ , (b)  $C_{rt}$ , (c)  $C_{rv}$ , (d)  $C_{tr}$ , (e)  $C_{tt}$ , (f)  $C_{vr}$ , (h)  $C_{vr}$  and (i)  $C_{vv}$  for the 3-D velocity structure with hard ocean bottom and variable bathymetry. Scholte and guided P-wave modes are highlighted by white and yellow arrows, respectively, while Love waves are denoted by green arrows. Black arrows represent cross-mode terms. The relative amplitudes between VSGs are not preserved; however, the scaling of each panel relative to  $C_{vv}$  is shown at the bottom of each panel.

subsurface investigations (Xia et al. 2003; Luo et al. 2007; Wu et al. 2020). However, the excitation of guided P waves—arising from variations in ambient source locations or bathymetry—truncates Scholte waves, thereby affecting their bandwidth and modal content. Suppressing or muting them prior to extracting the dispersion spectrum can extend the observable dispersive behaviour of the Scholte wave modes and increase their usable frequency range for inversion through dispersion images. As observed in the examples presented

above, the Scholte-wave dispersion spectra calculated from multicomponent cross-correlations can recover additional higher-order modes. Specifically, the  $\mathcal{C}_{rr}$  component captures more energy from higher-order Scholte wave modes, while the  $\mathcal{C}_{vv}$  from fundamental mode. Wang *et al.* (2022) demonstrated that the joint inversion of four-mode dispersion curves obtained from active-source (airgun), multicomponent OBN Scholte wave data can reduce the maximum inversion error by a factor of 16 compared to inversion using only

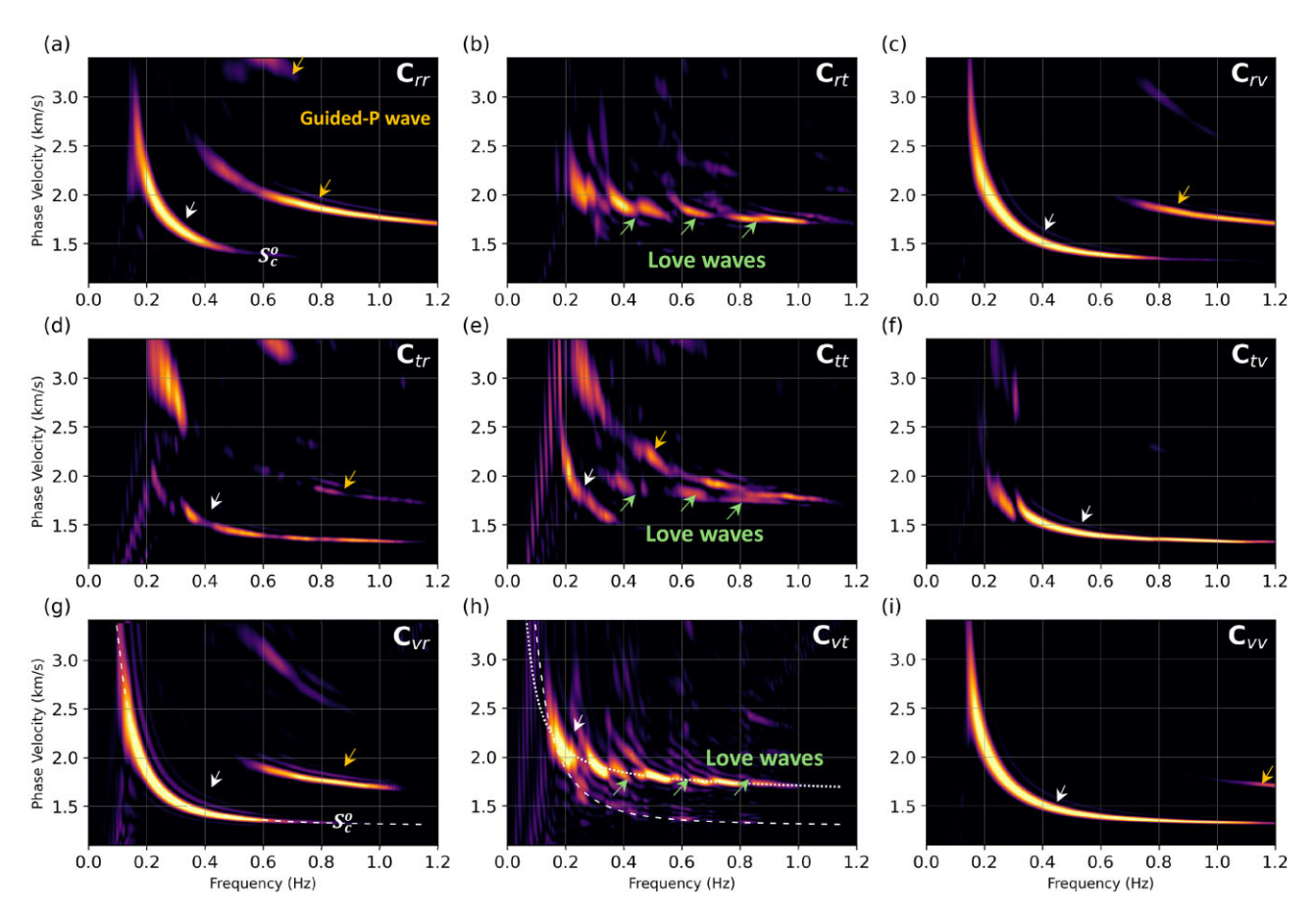


Figure 22. Dispersion panels for VSGs in Fig. 21. (a)  $C_{rr}$ , (b)  $C_{rt}$ , (c)  $C_{rv}$ , (d)  $C_{tr}$ , (e)  $C_{tt}$ , (e)  $C_{tv}$ , (g)  $C_{vr}$ , (h)  $C_{vt}$  and (i)  $C_{vv}$  components. Scholte and guided P-wave modes are highlighted by white and yellow arrows, respectively, while Love waves are denoted by green arrows. The theoretical fundamental Scholte mode (dashed curve) is plotted in panels (g) and (h), and the Love wave mode (dotted curve) is plotted in panel (h).

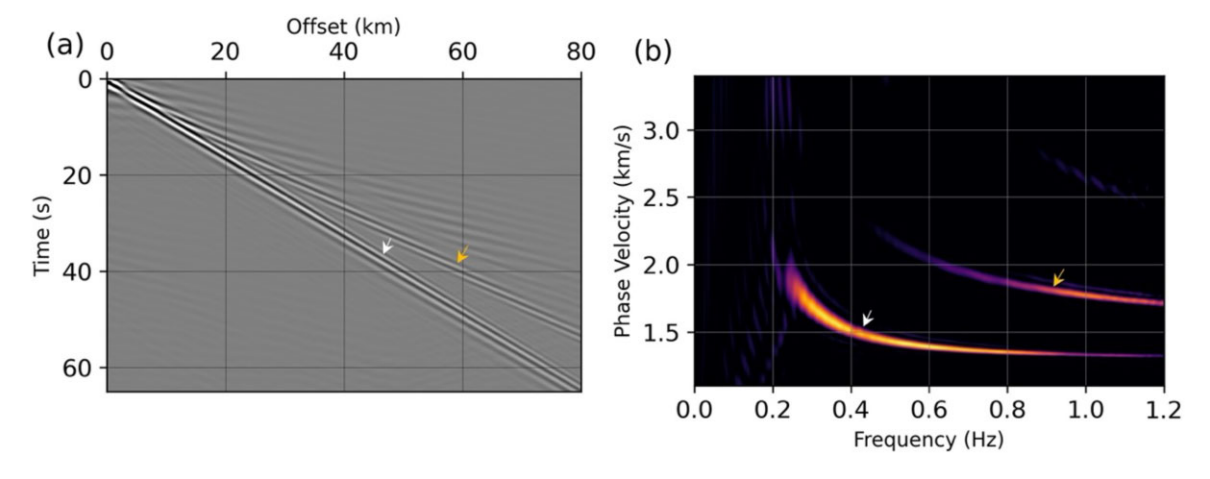


Figure 23. Pressure-to-pressure component  $C_{pp}$  (a) VSG and (b) Dispersion panel for the 3-D velocity structure with soft ocean bottom and variable bathymetry. Scholte and guided P-wave modes are highlighted by white and yellow arrows, respectively.

the fundamental mode. Compared to fundamental-mode-only inversion, joint inversion with higher-order modes effectively increases both the inversion depth and resolution. Multicomponent ambient cross-correlations recorded on OBNs provide a practical means to capture multiple Scholte wave modes for joint inversion to build low-frequency offshore elastic Earth models. These models can help accelerate convergence in FWI analyses of higher-frequency OBN data. In low-frequency surface-wave FWI applications, incor-

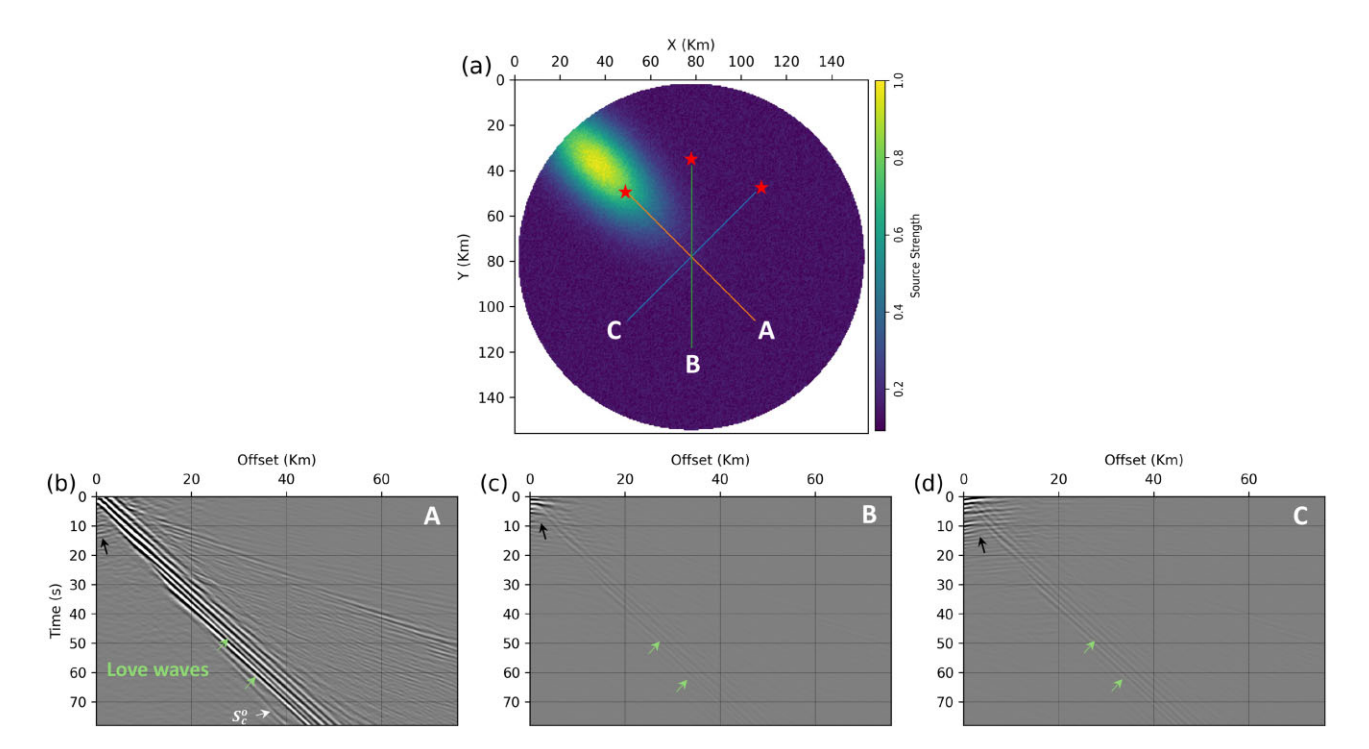


Figure 24. (a) Inhomogeneous secondary-microseism source distribution.  $C_{vt}$  VSG recorded on receiver line (b) A, (c) B and (d) C, as shown in panel (a). The amplitudes in the VSGs are relative.

porating guided *P*-wave modes—due to their interaction with the seabed and ability to carry shallow subsurface information—can improve resolution near the ocean bottom.

Another key observation is that not all VSG components are equally important. While OBN data theoretically can provide 16 different VSGs derived from pressure and three velocity components for each virtual shot point, not all components yield distinct information useful for inversion. VSGs with transverse components are particularly effective for Love waves, which are most prominently observed on the  $\mathcal{C}_{vt}$  VSG. The  $\mathcal{C}_{rr}$  VSG records higher-order Scholte modes most prominently, while  $C_{vv}$  and  $C_{pp}$ provide comprehensive observations of fundamental Scholte mode and guided P waves. Energy in the VSG components corresponding to the middle row and middle column of the VSG tensor- $\mathcal{C}_{rt}$ ,  $\mathcal{C}_{tr}$ ,  $\mathcal{C}_{tt}$ ,  $\mathcal{C}_{tv}$  and  $\mathcal{C}_{vt}$ —is generally significantly weaker than in the others. Collectively, VSGs with vertical components— $C_{vr}$ ,  $C_{vt}$  and  $\mathcal{C}_{vv}$ —along with  $\mathcal{C}_{rr}$  VSG, effectively capture all wave modes recorded on dense ocean-bottom sensors due to secondary microseismic sources.

### 5 CONCLUSIONS

We present a CCM methodology for ambient seismic wavefields recorded on dense arrays of ocean-bottom sensors. This CCM approach differs from traditional ambient wavefield cross-correlation modelling, which relies on Green's function retrieval assumptions, by offering a more flexible and accurate framework. Using this method, we simulate the cross-correlation wavefields for velocity and pressure components using 3-D Earth models and examine the impact of key first-order control factors within the context of ocean-bottom ambient seismology interferometric observations. These factors include the nature of the ocean bottom (i.e. soft versus hard), ambient source depth, ocean water column height,

ocean-bottom bathymetric variations and inhomogeneous ambient source distributions. These control factors influence the generation, propagation and energy partitioning of seismic waves, particularly surface waves (Scholte and Love waves) and guided *P*-wave modes at sub-1.0 Hz frequencies.

In the absence of ocean-bottom bathymetric variations and with only vertical velocity gradients in the 3-D Earth model, we identify two primary dispersive wave types in VSGs: Scholte waves and guided P-waves; Love waves are typically absent. Synthetic experiments reveal distinct differences in wave signatures depending on the location of the ambient energy sources and the oceanwater depths. Notably, the presence and dominance of guided Pwave modes increase with greater water depths, affecting the energy distribution and frequency content of Scholte waves. In contrast, when considering a vertically and laterally heterogeneous 3-D Earth model with significant bathymetric variations, Love waves are clearly observed with a more prominent presence in the  $C_{vt}$  VSG components. By examining the 3 × 3 velocity VSG tensor in soft ocean bottom scenarios, we find that higher-order Scholte modes are more prominently observed in the  $C_{rr}$  and  $C_{tt}$  VSG components. No higher-order Scholte modes are observed with a hard ocean bottom. Ambient energy sources near the ocean surface, typically associated with secondary microseism sources, generate significant guided P modes when the ocean-water depth exceeds the wavelength corresponding to the source frequency. In contrast, sources located near the seabed, characteristic of primary microseism sources, excite minimal guided P modes. Instead, the majority of source energy is concentrated in surface waves.

We also explore the effects of the heterogeneous distribution of secondary microseism sources in the presence of variable bathymetry and a heterogeneous Earth model on wave-mode excitation. The directional nature of the ambient source field—often characterized by azimuthal variations—strongly influences the amplitudes and characteristics of the resulting Love waves.

This is particularly evident in the VSGs derived from ocean-bottom receiver lines aligned along different azimuthal orientations relative to the source distribution. Strong Love waves are observed when the receiver lines align with the strongest source azimuthal orientation, supporting the hypothesis that Love waves are strongly generated in the source region through Rayleigh-to-Love wave conversion, especially in the presence of ocean-bottom bathymetric variations and lateral Earth structural heterogeneity.

Overall, these observations provide a deeper understanding of the complex ambient seismic wavefield in the ocean. They emphasize the importance of considering the effects of the various key control factors explored in this study when interpreting ocean-bottom ambient cross-correlation data. Ultimately, this enables the accurate modelling and inversion of low-frequency ambient data recorded on ocean-bottom sensors for low-frequency elastic velocity model building.

#### ACKNOWLEDGMENTS

We gratefully acknowledge the sponsors of the Mines Center for Wave Phenomena Consortium for supporting this research. We also thank the Wendian HPC cluster and Mines Research Computing, as well as the Kestrel HPC cluster at the National Renewable Energy Laboratory, for providing high-performance computing resources. The authors appreciate the developers of the open-source software SPECFEM3D Cartesian for their continued community work, with special thanks to Daniel Peter for his assistance in troubleshooting. We are also grateful to Dr. Roel Snieder for our thoughtful discussions, and to the two anonymous reviewers for their constructive suggestions, which helped improve this manuscript.

#### DATA AVAILABILITY

The SPECFEM3D model files (meshfem\_3D files) and the corresponding modelled data set presented in this study is openly available on Zenodo: https://doi.org/10.5281/zenodo.16941774. Further details about the data set, along with an illustrative example of ambient cross-correlation modelling, are provided at: https://github.com/padesh/OBN-Seismic-Interferometry-dataset.

#### REFERENCES

- Abrahams, L.S., Krenz, L., Dunham, E.M., Gabriel, A.-A. & Saito, T., 2023. Comparison of methods for coupled earthquake and tsunami modelling, *Geophys. J. Int.*, 234(1), 404–426.
- Aki, K. & Richards, P.G., 2002. Quantitative Seismology, 2nd edn, University Science Books.
- Ardhuin, F. & Herbers, T.H., 2013. Noise generation in the solid Earth, oceans and atmosphere, from nonlinear interacting surface gravity waves in finite depth, *J. Fluid Mech.*, 716, 316–348.
- Ardhuin, F., Gualtieri, L. & Stutzmann, E., 2015. How ocean waves rock the Earth: two mechanisms explain microseisms with periods 3 to 300 s, *Geophys. Res. Lett.*, 42(3), 765–772.
- Bensen, G., Ritzwoller, M., Barmin, M., Levshin, A.L., Lin, F., Moschetti, M., Shapiro, N. & Yang, Y., 2007. Processing seismic ambient noise data to obtain reliable broad-band surface wave dispersion measurements, *Geophys. J. Int.*, 169(3), 1239–1260.
- Bohlen, T., Kugler, S., Klein, G. & Theilen, F., 2004. 1.5 D inversion of lateral variation of Scholte-wave dispersion, *Geophysics*, **69**(2), 330–344
- Bromirski, P.D., Duennebier, F.K. & Stephen, R.A., 2005. Mid-ocean microseisms, Geochem. Geophys. Geosyst., 6(4), doi: 10.1029/2004GC000768.

- Bureau of Ocean Energy Management (BOEM), 2014. Northern gulf of mexico deepwater bathymetry grid derived from 3d seismic surveys. Available at: www.boem.gov/oil-gas-energy/mapping-and-data/map-gal lery/northern-goa-deepwater-bathymetry-grid-3d-seismic( 16 September 2025, Date accessed).
- Bussat, S. & Kugler, S., 2011. Offshore ambient-noise surface-wave tomography above 0.1 Hz and its applications, *Leading Edge*, **30**(5), 514–524.
- de Ridder, S. & Biondi, B., 2013a. Repeatability analysis of ambientseismic-noise tomography on four valhall datasets, 2004-2010, in SEG International Exposition and Annual Meeting, pp. SEG–2013, SEG.
- de Ridder, S. & Dellinger, J., 2011. Ambient seismic noise eikonal tomography for near-surface imaging at Valhall, *Leading Edge*, 30(5), 506–512.
- de Ridder, S.A. & Biondi, B.L., 2015. Ambient seismic noise tomography at ekofisk, *Geophysics*, 80(6), B167–B176.
- de Ridder, S. A.L. & Biondi, B., 2013b. Daily reservoir-scale subsurface monitoring using ambient seismic noise, *Geophys. Res. Lett.*, 40(12), 2969–2974.
- Du, S., Cao, J., Zhou, S., Qi, Y., Jiang, L., Zhang, Y. & Qiao, C., 2020. Observation and inversion of very-low-frequency seismoacoustic fields in the South China sea, *J. acoust. Soc. Am.*, 148(6), 3992–4001.
- Ermert, L., Sager, K., Afanasiev, M., Boehm, C. & Fichtner, A., 2017.

  Ambient seismic source inversion in a heterogeneous Earth: theory and application to the Earth's Hum, *J. Geophys. Res.: Solid Earth*, **122**(11), 9184–9207
- Fukao, Y., Nishida, K. & Kobayashi, N., 2010. Seafloor topography, ocean infragravity waves, and background Love and Rayleigh waves, J. Geophys. Res.: Solid Earth, 115(B4), doi: 10.1029/2009JB006678.
- Gao, L., Pan, Y. & Mao, W., 2025. Numerical study on the characteristics of guided waves in shallow marine environment, *J. Appl. Geophys.*, 237, 105 704.
- Girard, A.J., Shragge, J. & Olofsson, B., 2023. Low-frequency ambient ocean-bottom node surface-wave seismology: a Gulf of Mexico case history, *Geophysics*, 88(1), B21–B32.
- Girard, A.J., Shragge, J., Danilouchkine, M., Udengaard, C. & Gerritsen, S., 2024. Observations from the Seafloor: ultra-low-frequency ambient ocean-bottom nodal seismology at the amendment field, *Geophys. J. Int.*, 239(1), 17–36.
- Gregersen, S. & Alsop, L., 1976. Mode conversion of Love waves at a continental margin, Bull. seism. Soc. Am., 66(6), 1855–1872.
- Gualtieri, L., Stutzmann, E., Capdeville, Y., Ardhuin, F., Schimmel, M., Mangeney, A. & Morelli, A., 2013. Modelling secondary microseismic noise by normal mode summation, *Geophys. J. Int.*, 193(3), 1732–1745.
- Gualtieri, L., Stutzmann, É., Capdeville, Y., Farra, V., Mangeney, A. & Morelli, A., 2015. On the shaping factors of the secondary microseismic wavefield, J. Geophys. Res.: Solid Earth, 120(9), 6241–6262.
- Gualtieri, L., Bachmann, E., Simons, F.J. & Tromp, J., 2020. The origin of secondary microseism Love waves, *Proc. Natl. Acad. Sci. USA*, 117(47), 29 504–29 511.
- Halliday, D. & Curtis, A., 2008. Seismic interferometry, surface waves and source distribution, *Geophys. J. Int.*, 175(3), 1067–1087.
- Hasselmann, K., 1963. A statistical analysis of the generation of microseisms, Rev. Geophys., 1(2), 177–210.
- Haubrich, R.A. & McCamy, K., 1969. Microseisms: coastal and pelagic sources, Rev. Geophys., 7(3), 539–571.
- Herrmann, R.B., 2013. Computer programs in seismology: an evolving tool for instruction and research, Seismol. Res. Lett., 84(6), 1081–1088.
- Iyer, H., 1958. A study on the direction of arrival of microseisms at Kew Observatory, *Geophys. J. Int.*, **1**(1), 32–43.
- Kennett, B., 2023. Interacting seismic waveguides: Multimode surface waves and leaking modes, *Seismica*, **2**(1), doi: 10.26443/seismica.v2i1.282.
- Klein, G., 2003. Acquisition and inversion of dispersive seismic waves in shallow marine environments, *Ph.D. thesis*, Faculty of Mathematics and Natural Sciences, Kiel University, Germany.

- Klein, G., Bohlen, T., Theilen, F., Kugler, S. & Forbriger, T., 2005. Acquisition and inversion of dispersive seismic waves in shallow marine environments, *Mar. Geophys. Res.*, 26, 287–315.
- Komatitsch, D. & Tromp, J., 2002a. Spectral-element simulations of global seismic wave propagation—I. Validation, *Geophys. J. Int.*, **149**(2), 390– 412.
- Komatitsch, D. & Tromp, J., 2002b. Spectral-element simulations of global seismic wave propagation—II. Three-dimensional models, oceans, rotation and self-gravitation, *Geophys. J. Int.*, **150**(1), 303–318.
- Komatitsch, D., Barnes, C. & Tromp, J., 2000. Wave propagation near a fluid-solid interface: A spectral-element approach, *Geophysics*, 65(2), 623–631.
- Komatitsch, D. et al., 2023. Specfem/specfem3d: Specfem3d v4.1.0.
- Le Pape, F., Craig, D. & Bean, C.J., 2021. How deep ocean-land coupling controls the generation of secondary microseism Love waves, *Nat. Commun.*, 12(1), 2332.
- Li, Y.E. & Demanet, L., 2016. Full-waveform inversion with extrapolated low-frequency data, *Geophysics*, 81(6), R339–R348.
- Longuet-Higgins, M.S., 1950. A theory of the origin of microseisms, Phil. Trans. R. Soc. London Ser. A Math. Phys. Sci., 243(857), 1–35.
- Love, A. E.H., 1911. Some Problems of Geodynamics: Being an Essay to which the Adams Prize in the University of Cambridge was Adjudged in 1911, University Press.
- Luo, Y., Xia, J., Liu, J., Liu, Q. & Xu, S., 2007. Joint inversion of high-frequency surface waves with fundamental and higher modes, J. Appl. Geophys., 62(4), 375–384.
- Mordret, A., Landès, M., Shapiro, N., Singh, S., Roux, P. & Barkved, O., 2013. Near-surface study at the Valhall oil field from ambient noise surface wave tomography, *Geophys. J. Int.*, 193(3), 1627–1643.
- Nakata, N., Gualtieri, L. & Fichtner, A., 2019. Seismic Ambient Noise, Cambridge University Press.
- Ning, I. L.C., Tan, J. & Dash, R., 2024. Sparse ocean-bottom node seismic interferometry and inversion: a Gulf of Mexico study, in *Fourth Interna*tional Meeting for Applied Geoscience & Energy, pp. 1830–1834, Society of Exploration Geophysicists and American Association of Petroleum Geologists.
- Ólafsdóttir, E.A., Erlingsson, S. & Bessason, B., 2018. Tool for analysis of multichannel analysis of surface waves (MASW) field data and evaluation of shear wave velocity profiles of soils, Can. Geotech. J., 55(2), 217–233.
- Pandey, A., de Ridder, S., Shragge, J. & Girard, A.J., 2025. Ocean-bottom seismic interferometry in coupled acoustic–elastic media, *Geophys. J. Int.*, 242(3),ggaf271, doi: 10.1093/gji/ggaf271.
- Park, C.B., Miller, R.D. & Xia, J., 1999. Multichannel analysis of surface waves, *Geophysics*, 64(3), 800–808.
- Pekeris, C.L., 1948. Theory of propagation of explosive sound in shallow water.
- Ritzwoller, M.H. & Levshin, A.L., 2002. Estimating shallow shear velocities with marine multicomponent seismic data, *Geophysics*, 67(6), 1991–2004.
- Ruan, Y., Forsyth, D.W. & Bell, S.W., 2014. Marine sediment shear velocity structure from the ratio of displacement to pressure of rayleigh waves at seafloor, J. Geophys. Res.: Solid Earth, 119(8), 6357–6371.
- Sager, K., Ermert, L., Boehm, C. & Fichtner, A., 2018. Towards full waveform ambient noise inversion, *Geophys. J. Int.*, 212(1), 566–590.
- Saito, T., 2010. Love-wave excitation due to the interaction between a propagating ocean wave and the sea-bottom topography, *Geophys. J. Int.*, 182(3), 1515–1523.
- Scholte, J., 1947. The range of existence of Rayleigh and Stoneley waves, Geophysical Supplements to the Monthly Notices of the Royal Astronomical Society, 5(5), 120–126.
- Shapiro, N.M., Campillo, M., Stehly, L. & Ritzwoller, M.H., 2005. High-resolution surface-wave tomography from ambient seismic noise, *Science*, 307(5715), 1615–1618.

- Shi, C., Ren, H. & Chen, X., 2023. Dispersion inversion for *P* and *S*-wave velocities based on guided *P* and Scholte waves, *Geophysics*, 88(6), R721–R736.
- Shtivelman, V., 2004. Estimating seismic velocities below the sea-bed using surface waves, Near Surf. Geophys., 2(4), 241–247.
- Snieder, R., 2004. Extracting the Green's function from the correlation of coda waves: a derivation based on stationary phase, *Phys. Rev. E*, 69(4), 046.610
- Snieder, R., Wapenaar, K. & Larner, K., 2006. Spurious multiples in seismic interferometry of primaries, *Geophysics*, 71(4), SI111–SI124.
- Stehly, L., Campillo, M. & Shapiro, N., 2006. A study of the seismic noise from its long-range correlation properties, J. Geophys. Res.: Solid Earth, 111(B10), doi: 10.1029/2005JB004237.
- Stewart, P., 2006. Interferometric imaging of ocean bottom noise, in SEG International Exposition and Annual Meeting, pp. 1555–1559, SEG.
- Sun, C., Wang, Z., Wu, D., Cai, R. & Wu, H., 2021. A unified description of surface waves and guided waves with relative amplitude dispersion maps, *Geophys. J. Int.*, 227(3), 1480–1495.
- Sun, Y.-C., Zhang, W., Xu, J.-K. & Chen, X., 2017. Numerical simulation of 2-D seismic wave propagation in the presence of a topographic fluid– solid interface at the sea bottom by the curvilinear grid finite-difference method, *Geophys. J. Int.*, 210(3), 1721–1738.
- Tromp, J., Luo, Y., Hanasoge, S. & Peter, D., 2010. Noise cross-correlation sensitivity kernels, *Geophys. J. Int.*, 183(2), 791–819.
- Virieux, J. & Operto, S., 2009. An overview of full-waveform inversion in exploration geophysics, *Geophysics*, 74(6), WCC1–WCC26.
- Wang, Y., Li, Z., Geng, J., You, Q., Hao, T., Hu, Y., Zhao, C., Zhang, Y. & Liu, Y., 2020. Seismic imaging of S-wave structures of shallow sediments in the East China sea using OBN multicomponent Scholte-wave data, *Geophysics*, 85(6), EN87–EN104.
- Wang, Y., You, Q. & Hao, T., 2022. Estimating the shear-wave velocities of shallow sediments in the Yellow Sea using ocean-bottom-seismometer multicomponent Scholte-wave data, Front. Earth Sci., 10, 812 744. doi:10.3389/feart.2022.812744.
- Wapenaar, K. & Fokkema, J., 2006. Green's function representations for seismic interferometry, *Geophysics*, 71(4), SI33–SI46.
- Weaver, R.L. & Lobkis, O.I., 2001. Ultrasonics without a source: thermal fluctuation correlations at MHz frequencies, *Phys. Rev. Lett.*, 87(13), 134301.
- Webb, S.C., 1998. Broadband seismology and noise under the ocean, Rev. Geophys., 36(1), 105–142.
- Wu, G.X., Pan, L., Wang, J.N. & Chen, X., 2020. Shear velocity inversion using multimodal dispersion curves from ambient seismic noise data of USArray transportable array, J. Geophys. Res.: Solid Earth, 125(1), e2019JB018213, doi: 10.1029/2019JB018213.
- Xia, J., Miller, R.D., Park, C.B. & Tian, G., 2003. Inversion of high frequency surface waves with fundamental and higher modes, *J. Appl. Geophys.*, 52(1), 45–57.
- Xu, Z., Mikesell, T.D., Gribler, G. & Mordret, A., 2019. Rayleigh-wave multicomponent cross-correlation-based source strength distribution inversion. Part 1: theory and numerical examples, *Geophys. J. Int.*, 218(3), 1761–1780.
- Xu, Z., Stutzmann, É., Farra, V. & Crawford, W.C., 2025. Theoretical modelling of secondary microseisms considering source and receiver site structures, with a focus on ocean-bottom sediment effects, *J. Geophys. Res.: Solid Earth*, 130(5), e2024JB030767, doi: 10.1029/2024JB030767.
- Yang, Y. & Ritzwoller, M.H., 2008. Characteristics of ambient seismic noise as a source for surface wave tomography, *Geochem. Geophys. Geosyst.*, 9(2), doi: 10.1029/2007GC001814.
- Yao, H., Campman, X., de Hoop, M.V. & van der Hilst, R.D., 2009. Estimation of surface wave Green's functions from correlation of direct waves, coda waves, and ambient noise in SE Tibet, *Phys. Earth planet. Inter.*, 177(1–2), 1–11.